Co-option of neutrophil fates by tissue environments

Iván Ballesteros[1*¥], Andrea Rubio-Ponce[1,2*], Marco Genua[3¶], Eleonora Lusito[3¶], Immanuel Kwok[4¶], Gabriel Fernández-Calvo[5], Tariq E. Khoyratty[6], Erinke van Grinsven[6], Sara González-Hernández[1], José Ángel Nicolás-Ávila[1], Tommaso Vicanolo[1], Antonio Maccataio[1], Alberto Benguría[7], Jackson LiangYao Li[1,4], José M Adrover[1], Alejandra Aroca-Crevillen[1], Juan A. Quintana[1], Sandra Martín-Salamanca[1], Francisco Mayo[1], Stefanie Ascher[8], Giulia Barbiera[3], Oliver Soehnlein[9], Matthias Gunzer[10], Florent Ginhoux[4], Fátima Sánchez-Cabo[2], Estanislao Nistal-Villán[11], Christian Schulz[12,13] Ana Dopazo[7], Christoph Reinhardt[8], Irina A. Udalova[6], Lai Guan Ng[4], Renato Ostuni[3] and Andrés Hidalgo[1,9¥]

[1] Area of Cell & Developmental Biology, Centro Nacional de Investigaciones Cardiovasculares Carlos III, Madrid, 28029, Spain
[2] Bioinformatics Unit, Centro Nacional de Investigaciones Cardiovasculares Carlos III, Madrid, 28029, Spain
[3] Vita-Salute San Raffaele University, and San Raffaele-Telethon Institute for Gene Therapy (SR-Tiget), IRCCS San Raffaele Scientific Institute, Milan, 20132, Italy
[4] Singapore Immunology Nework (SIgN), A*STAR, Biopolis, Singapore 138648, Singapore
[5] Department of Mathematics & MOLAB-Mathematical Oncology Laboratory, University of Castilla-La Mancha, Ciudad Real, 13001, Spain
[6] Kennedy Institute of Rheumatology, University of Oxford, OX3 7FY, UK
[7] Genomic Unit, Centro Nacional de Investigaciones Cardiovasculares Carlos III, Madrid 28029, Spain
[8] Center for Thrombosis and Hemostasis Mainz (CTH), University Medical Center Mainz, Johannes Gutenberg University of Mainz, Mainz, 55131, Germany
[9] Institute for Cardiovascular Prevention (IPEK), Ludwig-Maximillians-Universitat, Munich, 80336, Germany
[10] Institute for Experimental Immunology and Imaging, University Hospital, University Duisburg-Essen, Essen, 445141, Germany
[11] Microbiology Section, Departament Pharmacological and Health Sciences, Facultad de Farmacia, Universidad CEU San Pablo, Madrid, 28668, Spain
[12] Medizinische Klinik und Poliklinik I, LMU Klinikum, Ludwig-Maximilians-Universität, Munich, 80336, Germany
[13] DZHK (German Centre for Cardiovascular Research), Munich, 80336, Germany

*, these authors contributed equally to this study
¶, these authors contributed equally to this study
¥ Corresponding authors

Lead contact: Andrés Hidalgo (ahidalgo@cnic.es)

Area of Cell & Developmental Biology, Fundación CNIC, Calle Melchor Fernández Almagro 3, 28029 Madrid, Spain. Phone: +34 91 4531200 (Ext. 1504). Fax: +34 91 4531245

Summary

Classically considered short-lived, purely defensive leukocytes, neutrophils are unique in their fast and moldable response to stimulation. This plastic behavior may underlie variable and even antagonistic functions during inflammation or cancer, yet the full spectrum of neutrophil properties as they enter healthy tissues remains unexplored. Using a new model to track neutrophil fates, we found short but variable lifetimes across multiple tissues. Through analysis of the receptor, transcriptional and chromatin accessibility landscapes, we identify varying neutrophil states and assign non-canonical functions, including vascular repair and hematopoietic homeostasis. Accordingly, depletion of neutrophils compromised angiogenesis during early age, genotoxic injury and viral infection, and impaired hematopoietic recovery after irradiation. Neutrophils acquired these properties in target tissues, a process that in the lungs occurred in CXCL12-rich areas and relied on CXCR4. Our results reveal that tissues co-opt neutrophils *en route* for elimination to induce programs that support their physiological demands.

Introduction

A fundamental property of myeloid leukocytes is their remarkable transcriptional and functional plasticity in response to environmental signals (Natoli and Ostuni, 2019). This plastic behavior has been demonstrated under both pathological conditions, as well as in the steady state, in which it manifests by the acquisition of phenotypic and transcriptional profiles that are unique to the tissue of residence (Lavin et al., 2015; Wynn et al., 2013). These tissue-associated features have been almost exclusively studied for macrophages, a population of cells that acquire similar tissue-tailored properties regardless of dissemination during embryonic and adult life, which indicated dominant roles for tissue-derived signals in harnessing the plasticity of precursor cells (erythro-myeloid progenitors or monocytes, respectively) to promote tissue-specific properties (Ginhoux and Guilliams, 2016). Illustrative of the relevance of this myeloid program, macrophages in the lungs, intestine and spleen, for example, adopt features that are needed for surfactant clearance, immune tolerance and iron recycling, respectively (Lavin et al., 2015). Because macrophages occupy tissues for extended periods of time, or even the full organismal lifetime, acquisition of tissue-specific functions are generally believed to demand long residence times.

Despite a shared myeloid origin, the possibility that neutrophils (the most abundant myeloid leukocytes) adopt tissue-restricted properties has remained unexplored. This knowledge gap is in large part caused by the belief that the neutrophil short life in the

circulation (Hidalgo et al., 2019) and reduced transcriptional activity preclude genetic adaptation to tissue environments (Silvestre-Roig et al., 2016). Existing evidence has shown, however, that cancer can instruct different transcriptional profiles, resulting in functions that can either promote, or counteract, tumoral growth and metastasis (Coffelt et al., 2016). Similar heterogeneous behavior has been reported in the context of stroke, myocardial infarction, autoimmune disease and infections (Cuartero et al., 2013; Gupta and Kaplan, 2016; Ma et al., 2016; Tsuda et al., 2004). Thus, we deemed it possible that *bona fide* neutrophil subsets existed also in healthy tissues, that they adopted properties tailored to the needs of those tissues, and that they fulfilled important, non-immune tasks for organismal physiology.

Here, we examined the diversification of neutrophil properties in tissues. We found that the lifetime of neutrophils in multiple tissues extends at least as long as their time in circulation thus providing time for adaptation to local environments, which we demonstrate by protein, transcript and epigenetic profiling. These analyses allowed us to identify non-canonical functions for neutrophils and to show that, in the lung, tissue-specific programming demands chemokine-guided positioning in instructing niches. Our findings demonstrate that, despite limited residence times in tissues, neutrophils can tailor their properties to support organ homeostasis.

Results

Short and variable lifetimes of neutrophils in tissues

The half-life of neutrophils in the murine circulation has been estimated to be about 12 hours (Pillay et al., 2010), but it remains unknown in tissues. To determine the lifetimes in peripheral tissues we first used a model of parabiosis, in which neutrophils derived from the partner mice were quantified after separation of the parabiotic partners (thereby interrupting the supply of partner-derived cells), and their lifetimes estimated by the disappearance kinetics from each tissue (Figure 1A and Fig.S1A). With the exception of the bone marrow, we found rapid decline in all tissues with plateaus reached as early as day 1 in lung and spleen, and by day 4 in blood and liver (Figure 1A). Although inflammatory artifacts induced by surgical separation could have extended the life of neutrophils in some tissues (Summers et al., 2010), this result suggested lifetimes of one day or less for most tissues.

To gain a more accurate resolution of neutrophils lifetimes in tissues, and to avoid surgery-induced inflammation, we generated a mouse model that allowed tracking individual waves of neutrophils. We inserted a tamoxifen-inducible Cre recombinase

(Cre^{ERT}) in the *Ly6g* locus, a gene highly specific for neutrophils (Fig.S1B; (Hasenberg et al., 2015)), and crossed the knock-in mice with the Rosa26-LSL-tdTomato reporter line (hereafter iLy6G^{tdTom}) to allow controlled induction of the tdTomato fluorescent protein in neutrophils (Figure 1B). This model allowed us to track synchronous waves of neutrophils released from the BM after a single dose of tamoxifen (Fig.S1B-D), and to measure the kinetics of appearance and disappearance of neutrophils in individual tissues after inducing recombination. The earliest peak of recombined tdTomato^{+} neutrophils was seen at day 2 in the BM, as expected by active granulopoiesis in this organ, and one day later in all other tissues tested, including blood, liver, lung, spleen, intestine and skin (Figure 1B). By focusing on the disappearance rates starting from the peak of tdTomato^{+} neutrophils in each tissue, we put forward a mathematical model capturing the kinetics of labeled post-mitotic neutrophils (Fig.S1E). In our model we considered that neutrophils originated form the BM and seeded the rest of the tissues. We found variable half-lives depending on the tissue, with the shortest times in liver (8.71 hours) and the longest in skin (18.4 hours), whereas the blood yielded values of ~10 hours that were comparable to those obtained using isotopic labeling (Pillay et al., 2010); Figure 1B). We did not consider the values in the BM (20.2 hours) because they reflect both maturation and egress of neutrophils into blood, rather than just elimination of those that infiltrate the marrow from blood. These results indicated that neutrophils are not immediately eliminated when they enter tissues, but remain there for periods than can extend even longer than one day (when considering mean lifespans, ranging from 28 to 61 hours; see Methods and Fig.S1E).

Because certain tissue-resident myeloid cell types, including macrophages and mast cells, can originate from embryo-derived precursors (Gomez Perdiguero et al., 2015; Hoeffel et al., 2015; Li et al., 2018), we additionally used our fate-mapping model to ask whether embryonic Ly6G^{+} precursors could give rise to long-lived neutrophils in tissues. To this end, we treated iLy6G^{tdTom} mice with tamoxifen at E15.5 (a time at which fetal liver progenitors are already present; (McGrath et al., 2015)) and followed the presence of labeled neutrophils in several tissues at postnatal days 1 (P1) and 7 (P7). While tdTomato^{+} neutrophils were detectable in most tissues at low but reproducible levels at P1, we failed to find labeled cells at P7 (Figure 1C), suggesting that neutrophils detected in postnatal tissues are derived from definitive medullary hematopoiesis. We could confirm this observation by fate mapping at E8.5 using the *Csfr1*^{MeriCreMer} mouse model ((Gomez Perdiguero et al., 2015)**;** not shown).

Tissue-associated profiles of neutrophils identified by single cell analyses

Because our estimates revealed residence times in the range of tens of hours in tissues, with successive waves infiltrating every circadian cycle (Casanova-Acebes et al., 2018), we predicted that neutrophils might acquire distinct properties in each tissue. To examine this possibility, we first determined receptor expression by simultaneous labeling with 39 antibodies followed by mass cytometric and dimensionality reduction analyses (Fig.S2A-B). We focused on several leukocyte subsets to allow comparison of expression profiles in the BM, blood, spleen, lung, intestine and skin. Using the t-distributed stochastic linear embedding (tSNE) reduction algorithm we generated a bidimensional plot that contained neutrophils identified as $CD11b^+$ $Ly6G^+$, as well as various populations of macrophages ($F4/80^+$ $CD11b^+$, $SiglecF^+$ $CD11C^+$ and $CX3CR1^+$ $MHC\text{-}II^+$ $Ly6C^-$ for various tissues, the lung or the intestine, respectively), $CD115^+$ $CD11b^+$ monocytes, $CD19^+$ B cells, and $CD49d^+$ $NK1.1^+$ NK cells (Figure 2A and Fig.S2C), that distributed in 36 clusters (Fig.S2C). We found that, among all leukocytes, macrophages displayed the largest variability with discrete clusters that almost completely overlapped with individual tissues (Figure 2B), as expected from the divergent properties of these cells in organs (Wynn et al., 2013). Importantly, neutrophils also displayed cluster-to-tissue distributions (Figure 2C), to a higher extent than monocytes, B and NK cells (Fig.S2D). Indeed, we found distinct clusters for blood, lung and BM neutrophils, whereas intestinal and skin neutrophils clustered together, and the spleen overlapped with the marrow and the lung (Figure 2D and Fig.S2B). Thus, within the limitations of our preset marker panel, these data revealed marked phenotypic heterogeneity of neutrophils across tissues in the steady state.

To extend these findings and to confirm them at the transcriptional level, we profiled neutrophils from tissues by single cell RNA sequencing (scRNA-seq). As in the mass cytometric analysis, we intentionally processed a mix of leukocytes since we noted that isolated neutrophils performed worse in the single cell platform (see Methods for the criteria for neutrophil annotation; and Fig.S2E). We could not obtain sufficient neutrophils for analysis from the intestine or skin, and therefore focused on the other four tissues (BM, spleen, blood and lungs). Of 7490 neutrophils sequenced in our dataset, 6800 were from the BM, whereas only 380, 264 and 147 were from the spleen, blood and lungs, respectively, likely reflecting the strong drop in transcript levels as neutrophils mature and leave the marrow (Hoogendijk et al., 2019). Unbiased analysis of the neutrophil dataset identified 5 clusters (Fig.S2F), of which clusters 0, 1 and 2 were enriched in neutrophils from the BM and spleen, whereas clusters 3 and 4 were enriched in

neutrophils from blood and lungs, respectively (Figure 2E and Fig.S2F-G). Differentially expressed genes across clusters evidenced a transcriptional program associated with neutrophil maturation in the BM and spleen, as shown by the presence in cluster 0 of genes associated with S or G2/M phases of the cycle, including *mki67* and *Cdk1*, as well as transcripts associated with the synthesis of primary granules such as *Mpo*, *Elane* or *Ctsg*. Cluster 0 also included regulators of proliferation or early granulocytic differentiation, such as *Ms4a3* (Liu et al., 2019) and *Cebpe* (Evrard et al., 2018), altogether suggesting that this cluster identified cells at the promyelocytic stage in BM and spleen (Grassi et al., 2018) (Figure 2F, Fig.S2F-I and Table S1). Consistent with the maturational changes across clusters, the gene signature of immature granulocyte-macrophage progenitors (GMP) projected in Cluster 0, while the more committed proNeu and preNeu signatures (Evrard et al., 2018; Kwok et al., 2020) appeared in the transition from cluster 0 to 1 (Fig.S2J-L). In contrast to cluster 0, clusters 1-4 were predominantly post-mitotic, with clusters 1 and 2 enriched in the expression of genes encoding for secondary granule proteins (*Ltf, Chil3* or *Mmp8*) and maturation-associated genes such as *Cxcr2* (Evrard et al., 2018). Most of these genes, with the exception of *Cxcr2*, disappeared in clusters associated with the lung and blood (Figure 2F, Fig.S2G-I and Table S1). A similar behavior was observed for *Cebpe*, a transcription factor indispensable for secondary and tertiary granule formation (Bartels et al., 2015). Finally, upregulation of genes associated with mature neutrophils and immune defense such as *Ccl5*, *Cxcr2* and *Il1b* were predominantly expressed in clusters 3 and 4 (Figure 2F). The transcriptional profile of lung neutrophils reinforced the expression of blood-associated transcripts such as *Il1b* or *Ptgs2*, and further acquired the expression of new genes such as *Vegfa* and *Tnfaip3* (Figure 2F and Fig.S2I). A diffusion map of the neutrophils single cell transcriptomes also supported a continuous cell-state transition from the bone marrow and spleen to the blood, and finally to the lung (Fig.S2M).

Transcriptional and chromatin adaptations of tissue-infiltrating neutrophils

To further explore neutrophil heterogeneity and to gain depth in our transcriptomics analyses, we next performed bulk RNA-sequencing of neutrophils isolated from various tissues, including BM, blood, spleen, lung, intestine and skin. Although the abundance and distribution of neutrophils was unique for each of these tissues in the steady state (Fig.S3A-C and (Casanova-Acebes et al., 2018)), we could obtain enough cells from all tissues except for the liver, in which the quality of the RNA extracted from neutrophils was consistently poor (not shown). To refine our analyses, we used a parabiosis system

that enabled purification of neutrophils that had entered the tissues of the partner mouse, thereby allowing us to exclude those generated locally, particularly in granulopoietic organs such as the bone marrow and spleen (Figure 3A). Consistent with the single cell analyses, and despite normal granulocytic morphologies, we identified distinct transcriptional profiles in each tissue (Figure 3A and Table S2). An UpSet plot revealed poor transcriptional interactions between tissues, with the highest number of transcripts shared between the lung and intestine, and the highest expression of unique differentially expressed genes found in the skin and the intestine (Figure 3B). Of note, control experiments in which neutrophils from the different tissues were exposed to the same isolation method resulted in similar preferential expression of signature genes as those obtained in the RNA sequencing analyses (Fig.S3D). Likewise, inhibition of *de novo* transcription of lung neutrophils throughout the isolation procedure did not prevent the preferential expression of signature transcripts relative to blood (not shown), indicating that tissue processing and cell isolation did not introduce artifacts in our analyses. Interestingly, we found that the tissue-specific transcriptional signatures involved ~1 to 6.5% of the neutrophil transcriptome, a range that was within that of tissue-resident macrophages (1.3-3%, as estimated from (Lavin et al., 2014)).

We found good correlation between gene expression in tissues from the single cell and bulk sequencing analyses, as the top differentially expressed genes were found in both datasets, including genes of granule proteins in the BM, *Ifitm* genes in blood and *Il1b* in lung (Figure 3A and Fig.S2H). Projection of the bulk tissue profiles onto the scRNA-seq dataset confirmed consistent profiles, with clusters associated to the BM, blood and lung showing enrichment in single cells from the corresponding tissues (Figure 3C). In contrast, the bulk signatures from the intestine and skin did not identify cells sequenced from the other tissues, nor did the spleen as expected from this organ being largely embedded within the BM cluster and lacking a distinct signature (Figure 2E). Altogether, these data indicated that neutrophils acquire transcriptional properties associated with the tissues that they infiltrate in the steady state.

Although our findings revealed tissue-restricted profiles at the level of protein or gene expression, they did not demonstrate stable modifications in the neutrophil genome. To explore if this was the case, we assessed regions of chromatin accessibility in neutrophils isolated from the BM, blood, spleen and lungs by ATAC-sequencing. Principal component analysis of the accessible regions revealed marked diversity associated with the tissue of origin (Figure 3D). The biggest differences were apparent in the transition from BM or spleen into blood, in agreement with previous observations (Grassi et al.,

2018). However, changes in accessible chromatin were also prominent when comparing blood and lung (Figure 3E), suggesting chromatin modifications also in the transition from the circulation into tissues. K-means clustering of differentially open regions identified four clusters, with similar patterns at key neutrophil gene loci such as *S100a8* and *S100a9* across tissues (Figure 3F and Fig.S3E). Clusters 1 and 3 were associated with chromatin regions that changed their accessibility in lung neutrophils (C1, down; C3, up). Cluster 2 contained regions that gained accessibility in blood neutrophils, whereas cluster 4 was enriched in regions found in splenic neutrophils. Importantly, the affected regions within each cluster involved genes that had been detected in our bulk sequencing analyses (compare Figure 3A and Figure 3F) and, in particular, cluster 3 included open chromatin regions that projected well over the lung cluster in our single cell dataset (Figure 3G). Examination of motif enrichment across clusters identified general myeloid regulators such as PU.1 in cluster 1 that was, however, present in all clusters. In contrast, more restricted transcription factors like JunB were only enriched in cluster 3 (Fig.S3F). Finally, we found that changes in chromatin and transcriptome impinged on the expression of the identified genes at the protein level; for example, expression of CD74 and CR2 was elevated in splenic neutrophils, and CD14 and IL1β were higher in neutrophils from the lungs (Figure 3H-I).

Altogether, these data identified remarkable heterogeneity on neutrophils under steady-state conditions at the chromatin, RNA and protein levels. They also implied that neutrophil diversity is not only the consequence of medullary maturation, as their phenotypic and transcriptional diversity was further tuned when neutrophils entered peripheral tissues.

Neutrophil fates are imprinted in tissues

Whereas macrophage diversity is likely the consequence of long-term residence in tissues and extended exposure to local cues (Gosselin et al., 2014; Lavin et al., 2014), this was unlikely to be the cause of neutrophil diversification in tissues given their short lifespans (Figure 1). To examine the potential source of neutrophil specification, we first queried if the transcriptional patterns in tissues were already present in circulating cells, as this would imply remote pre-specification and deterministic homing to target tissues as proposed, for example, in the context of lung adenocarcinoma (Engblom et al., 2017). To this end we projected the signatures of each tissue onto the single cell transcriptome of blood neutrophils. As expected, the blood signature was strongest among all tested tissues (BM, blood, spleen, lung, intestine and skin) (Figure 4A). In contrast, no distinct

individual cells from blood displayed signatures from spleen, lung, intestine or skin neutrophils. Only a separate cluster of blood cells scored high for the BM signature (Figure 4A), but these likely represented newly marrow-released neutrophils as they expressed high levels of granule-related genes that are characteristic of granulocytic precursors (Fig.S4A).

In our bulk sequencing analysis of differentially expressed genes, we noticed that the lung, intestine and skin were transcriptionally more diverse, yet more similar with each other when compared with those from BM, blood and spleen (Fig.S4B). This raised the possibility that the transcriptional properties of these barrier tissues might be influenced by the commensal microbiota to which they are naturally exposed. We therefore assessed the transcriptional signature in germ-free mice of neutrophils from the blood, spleen and lung, as representative tissues from the two groups (Figure 4B), since we found that germ-free mice were virtually devoid of neutrophils in the intestine and skin (not shown). We found that the lack of microbiota had virtually no impact on the transcriptome of lung or splenic neutrophils (Figure 4B), and only moderate changes (667 differentially expressed genes) were found in blood neutrophils from control versus germ-free mice (Figure 4B, Fig.S4C and Table S3). Thus, the microbiota affects neutrophils in blood, but not their specification in the tested tissues, including the lung and spleen.

Given the lack of evidence for neutrophil programming in the circulation, we asked whether their signatures were imprinted when the cells reached each tissue, regardless of their origin. To this end, we first used a model of parabiosis and compared the phenotype of host-derived cells with that of partner-derived cells in the BM, blood, spleen and lung through multi-parametric mass cytometry. The parabiosis strategy was necessary to discriminate neutrophils reaching the tissue from the circulation (partner-derived) from those residing or generated in the tissue (host-derived). Projection of host and partner cells in a tSNE space revealed that neutrophils acquired the same tissue-specific profile, independent of their host or circulating origin (Figure 4C). The tissue-specific patterns became further evident when comparing the distribution of the cells into the different clusters defined by their cytometric profile in each tissue (Figure 4D and Fig.S4D), suggesting that specification of neutrophil signatures occurred in tissues.

To further confirm this possibility, we next performed transfer experiments in which BM neutrophils were injected into the lung or the spleen, thus bypassing the circulatory stage and allowing us to examine the phenotypic conversion of neutrophils exposed to a new environment. Of note, despite the artificial routes of administration we found that

neutrophils transferred to the spleen localized in the red pulp, near endogenous splenic neutrophils, and that a fraction of intratracheally-administered neutrophils migrated to the lung parenchyma, near host-derived neutrophils (not shown). Thus, in neutrophils recovered 16 hours after transfer we analyzed the cytometric profile of a small collection of markers previously found to vary across tissues, namely Ly6C, CD11b, CXCR2 and CD74. We found that, after only several hours in the tissues, BM neutrophils acquired the marker profile characteristic of neutrophils naturally residing in each tissue; for example, neutrophils transferred to the spleen were most similar to splenic neutrophils based on these markers, while those transfer to the lungs where closest to pulmonary neutrophils (Figure 4E). Time-dependent analyses of changes at the protein level revealed rapid (3 hours) upregulation of CXCR2, Il1β and CD11b after neutrophil transfer, whereas changes in CR2, CD74 and CD14 levels were only evident after 16h (Fig.S4E). We obtained similar results for the transcriptional signature of BM neutrophils transferred to lungs (Figure 4F and Fig.S4F); the cells rapidly lost the expression of BM-associated genes (e.g., *Cebpe* or *Ltf,* see Fig.S4G) and gained the expression of lung-associated genes (such as *Ptgs2* or *Il1b*), but not blood-type genes (*Ifitm3*; Figure 4F and Fig.S4F). Importantly, acquisition of this lung-type profile was specific because transfer of BM neutrophils into the peritoneum resulted in loss of the BM signature, without gain of a lung profile (Fig.S4H).

Finally, we asked whether the signature instructed by the lung, as a prototypical tissue, was dominant or not over pathological states. We took advantage of an existing scRNA-seq dataset of lung neutrophils in the presence of adenocarcinoma (Zilionis et al., 2019), in which we could identify two populations of neutrophils in healthy vs. tumor-bearing lungs (Fig.S4I). Projection of our tissue signatures onto this dataset was, as expected, stronger for pulmonary neutrophils (Fig.S4J), however it was unable to discriminate tumor-free versus tumor-associated neutrophils, even if the tumoral group presented evidence of what appeared to be a more immature state, based on the expression of granule-related genes (Fig.S4K). This finding suggested that, at least in this particular pathological scenario, the tissue (lung) imprints the neutrophil profile even in the presence of a pathological perturbation (adenocarcinoma). All combined, these data supported a model whereby neutrophil reprogramming occurs rapidly (within the scope of their lifetime in tissues, as defined in Figure 1), once the cells enter the tissues.

Angiogenic properties of neutrophils in the lung and intestine

The diversity of phenotype and transcriptome in each tissue suggested that, like macrophages, neutrophils may acquire functions that are distinct and tailored to the demands of each tissue. To gain insights into these potential functions we performed *in silico* analyses of the transcriptional signatures found in our bulk RNA-seq dataset (Figure 3A and Table S4). We found that pathways classically ascribed to neutrophils, such as those related to cell migration and immune responses, were only dominant in hematopoietic organs, especially BM and blood (Figure 5A). This observation was important because these two tissues have been the source of most studies examining neutrophil function. Homeostasis of leukocytes was also a prominent pathway of neutrophils from blood and BM, while B cell homeostasis was largely restricted to neutrophils of the spleen. The prediction in the spleen was supported by the expression of factors that promote lymphocyte activation and proliferation (Fig.S5A), and was in good agreement with previous reports (Puga et al., 2011).

To validate these predicted functional pathways we used a model of neutrophil depletion mediated by conditional expression of the diphtheria toxin (DT) receptor under the human *MRP8* promoter (Passegue et al., 2004), and induced by DT treatment (*MRP8*^{CRE}; Rosa26^{iDTR}; Fig.S5B). Repeated DT injection for up to one week profoundly reduced neutrophil counts in BM, blood and spleen, but did not deplete any other leukocyte populations in the steady state or cause infection (Fig.S5C-D). Importantly, however, depletion of neutrophils after sub-lethal irradiation caused strong impairment in the recovery of most hematopoietic lineages, including eosinophils, monocytes, B and T lymphocytes, NK cells and macrophages as detected in the blood, BM or spleen (Fig.S5D). This correlated with exacerbated spleen atrophy (Fig.S5E) and loss of lymphoid areas in the marrow and spleen after irradiation (Fig.S5F), altogether suggesting that neutrophils support hematopoietic recovery following genotoxic injury.

In contrast to hematological organs, pathway analyses of neutrophils in the lung, intestine and skin did not assign hematopoietic-supportive properties, but instead uncovered other non-canonical functions (Figure 5A). Specifically, regulation of vascular and axonal growth were strongly associated with the transcriptional signature of neutrophils from the lung and intestine, and epithelial growth by neutrophils from the skin (Figure 5A). We focused our attention on the lung, because we obtained consistent results from the single cell and bulk analyses (including chromatin accessibility), and because pulmonary neutrophils could be purified in high numbers for additional analysis. Consistent with the predicted angiogenic signature, we found genes involved in vascular

growth and repair (including *Apelin*, *Adamts* or *Vegfa*) that were significantly higher expressed in the lung in our bulk sequencing, and some of those genes were, as expected, also detectable in intestinal neutrophils (Figure 5B, Fig.S5G and Table S2). Examination of an angiogenic score (see Methods and Table S5) against our single cell dataset revealed that, among all leukocyte subsets, only neutrophils displayed such lung-specific profile (Figure 5C), suggesting that this was not a general effect of the lung environment but rather an exclusive property of neutrophils in this organ. Even in our single cell dataset, in which low-expressed transcripts are typically undetected, we could find differential expression of several genes involved in vascular repair (Figure 5D). Of note, we also found CD49d^{+} neutrophils, which have been previously assigned proangiogenic properties in the context of hypoxia (Massena et al., 2015), in the lungs but not in the intestine, indicating only partial overlap with our population (Fig.S5H).

We next assessed the contribution of neutrophils to pulmonary vascularization in the inducible neutropenia mouse model. We did not find vascular anomalies in the lungs of adult mice after 7 days of neutrophil depletion, both by histology (Fig.S5I) or when assessing endothelial proliferation (Figure 5E). We considered, however, alternative contexts that demand enhanced angiogenesis, such as organismal growth at young age, or after genotoxic injury induced by irradiation. In these contexts, depletion of neutrophils resulted in complete loss of proliferative capacity of endothelial cells (Figure 5E). We found a similar pro-angiogenic effect in the intestine of young mice (Figure 5F), but not in the spleen or the BM (Fig.S5J), as predicted by the pathway analysis. Finally, because the distribution of neutrophils in the adult intestine has been shown to be largely restricted to areas around isolated lymphoid follicles (ILF) (Fig.S5K and (Casanova-Acebes et al., 2018), we examined whether vascularization of these particular regions of the gut might be affected by neutropenia. Indeed, while the general architecture of the gut was not affected by neutrophil depletion (Fig.S5L), we found significant loss of vessels inside the ILF, but not in the surrounding submucosal area (Figure 5G). Altogether, these results indicated that neutrophils support homeostatic and stress-induced angiogenesis in tissues (lung and intestine) that instruct this particular transcriptional program.

CXCR4 guides neutrophils to sites of tissue-specification in the lung

We finally sought to understand the mechanisms that drive re-programming of neutrophils in tissues. We focused on lung neutrophils as they featured a distinct,

consistent profile in all our analyses. We used a screening approach in which we analyzed the transcriptional profile of lung neutrophils (composed of 37 genes, of which 8 are shown in Figure 6A), and those from blood for reference, using Nanostring technology. We first used function-blocking antibodies against TGF-β or GM-CSF, as these cytokines have been involved in neutrophils programming towards pro- and anti-tumoral functions, respectively (Engblom et al., 2017; Sagiv et al., 2015; Singhal et al., 2016), however none of the treatments altered the acquisition of the pulmonary signature (Figure 6A). We also profiled mice in which neutrophils lacked Bmal1, a master clock regulator involved in neutrophil infiltration of tissues (Adrover et al., 2019), and Nr4a1, an orphan nuclear receptor required for monocyte differentiation (Hanna et al., 2011) that we found consistently represented in the transcriptional and chromatin accessibility profiles of lung neutrophils (Figure 3F and Fig.S2H). Absence of Bmal1 caused a small reduction in the expression of signature genes but this was very variable (Figure 6A) and could not be reproduced by bulk RNA sequencing (not shown). Deletion of *Nr4a1*, in turn, partially affected the expression of only two of the analyzed genes (*Il1b* and *Ptgs2*; Figure 6A and Fig.S6A) but did not affect the vascular response in the lungs after irradiation (Fig.S6B), indicating minor or redundant roles for this factor in the specification of neutrophils in the lung.

We finally tested mice with neutrophil-specific deletion of *Cxcr4* (*MRP8*^{CRE}; CXCR4$^{fl/fl}$ referred herein as CXCR4$^{\Delta N}$), as the CXCL12-CXCR4 axis has been involved in the retention of neutrophils in lungs (Devi et al., 2013). Notably, the Nanostring analyses revealed that neutrophils lacking this receptor completely lost the pulmonary signature, while maintaining a normal profile for neutrophils in blood (Figure 6A-B). Confocal imaging of lungs from *Cxcl12* reporter mice, which marks cells expressing the ligand for CXCR4 with GFP, revealed patchy expression of CXCL12 that was largely restricted to larger vessels (Figure 6C and Fig.S6C). We found that neutrophils localized proximal to these CXCL12+ vessels in the lung, often establishing contacts with endothelial cells at the tip of the GFP clusters (Figure 6C, inset), suggesting that these might represent areas of neutrophil reprogramming. Interestingly, intratracheally-delivered neutrophils also localized near CXCL12+ vessels (Fig.S6D), suggesting general tropism of neutrophils towards these areas.

We next analyzed these mice under conditions that induced vascular proliferation. Consistent with the findings in mice depleted of neutrophils, CXCR4$^{\Delta N}$ mice displayed blunted proliferation after irradiation (Figure 6D) despite elevated neutrophil numbers in lungs (not shown). Interestingly, these mice also recapitulated the vascular aplasia in

intestinal ILF seen in neutropenic mice (Figure 6E and Fig.S6E). Because the lung is a common target of viral infections and neutrophils have been proposed to perform immune-patrolling functions in this organ (Yipp et al., 2017), we next subjected the mice and their controls (Cre^{NEG}; $CXCR4^{fl/fl}$) to infection with low doses of the influenza A virus. Despite no difference in survival rates, these mice presented significant loss of pulmonary vascularization 14 days post-infection (Fig.S6F-G), indicating additional roles for lung neutrophils in vascular repair after an infection.

Overall, our data suggested that neutrophils followed CXCL12/CXCR4 cues to reach areas of re-programming in the lung. Consistent with this possibility, intravital imaging revealed multiple defects in the migration of CXCR4-deficient neutrophils within the lungs (Figure 6F, Fig.S6H and Video S1), and reduced accumulation in this organ when adjusted to their numbers in blood (Figure 6G). The migratory defects seen in CXCR4 mutant mice were confirmed by tracking individual lung neutrophils in wild-type mice before and after exposure to a CXCR4 antagonist (AMD3100; not shown). To unambiguously assess if the defective specification of CXCR4-deficient neutrophils was caused by a disrupted ability to "find" instructing CXCL12+ niches, we transferred marrow neutrophils directly into lung intratracheally and then assessed their transcriptional profile compared with non-transferred BM cells, or with pulmonary neutrophils from the host. We found that, under these conditions, the transferred $CXCR4^{\Delta N}$ neutrophils gained normal expression of hallmark pulmonary genes (*Ptgs2*, *Il1b* and *Nr4a1*; Figure 6H), thus indicating that CXCR4 signaling is dispensable for transcriptional specification, but is needed to guide neutrophils to sites of reprogramming. We conclude that, at least in the particular case of the lungs, tissue-derived signals guide neutrophils to specific areas where they acquire their distinct phenotypic and functional properties.

Discussion

The realization that macrophages adapt to tissue environments represented a milestone towards better appreciating the physiological, non-immune roles of the innate immune system (Gosselin et al., 2014; Lavin et al., 2014). Indeed, the remarkable adaptation of these cells has been instrumental to define the function of myeloid cells as they specialize in supporting basal tissue functions, adaptation to stress, and that can even underlie pathological states (Keren-Shaul et al., 2017; Mass et al., 2017). Notably, however, macrophages are not the only or even more numerous myeloid cells found in tissues in the steady-state, as we and other have reported the presence of neutrophils

in virtually every analyzed tissue (Becher et al., 2014; Casanova-Acebes et al., 2018). Here, we show that neutrophils are not immediately eliminated as they enter naïve tissues, but remain there for periods than can extend for even longer than one day, and acquire remarkable heterogeneity at the chromatin, RNA and receptor levels. We find that this tissue-driven adaptation occurs rapidly in the new environment, possibly in dedicated microanatomical niches as illustrated in the lungs, where they gain distinct phenotypic and functional properties, including support of vascular homeostasis and hematopoietic recovery. Our study therefore expands the concept of myeloid plasticity, a concept so far only explored in detail for macrophages, by demonstrating remarkable neutrophil adaptability to different environments, thereby unveiling a biological property of neutrophils with important implications in innate immunity and tissue physiology.

A historical limitation when studying the homeostatic features of neutrophils has been their low numbers in the majority of tissues (Casanova-Acebes et al., 2018), the inability to expand or to maintain them in culture, and their reduced transcriptional activity (Silvestre-Roig et al., 2016), all of which may explain the lack of systematic exploration of their diversity in naïve organs. Consequently, a shortcoming of our study is that we restricted our in-depth analyses to neutrophil-rich tissues, including the BM, blood, spleen and lung, and additionally performed bulk transcriptomic characterization of neutrophils from the intestine and the skin. In these tissues, we focused our efforts on defining the acquisition of a distinct receptor repertoire and transcriptome profiles, and to show that the rapid changes in these properties once they enter tissues are matched by stable epigenetic modifications.

The consistent results obtained from complementary assays (bulk and single cell RNA sequencing, and mass cytometry) provided independent confirmation of the specific signatures of neutrophils in each tissue. Combination of bulk sequencing and mass cytometry with parabiosis, in turn, suggested that these signatures were acquired as neutrophils infiltrated the tissues from the bloodstream, an issue of particular relevance for tissues in which neutrophils are produced (i.e., bone marrow and spleen). In this regard, we note that myeloid progenitors crossing between parabiotic partners could potentially generate noise in this model, however we have found that crossed hematopoiesis represents less than 5% and should have a minor influence in the overall profiling of the cells.

As our transcriptomic analyses predicted distinct functional properties for each examined tissue, we performed functional validation of these functions in the lungs and intestine, as neutrophils from this organ featured signatures that consistently suggested a role in

angiogenesis. A remarkable finding was that the predicted transcriptional features of tissue neutrophils appeared to generally support housekeeping functions of the tissue from which they were extracted, such as hematopoietic homeostasis in the marrow, or epithelial growth in the skin, which will need further validation. Another unexpected finding was that the migratory and immune functions classically ascribed to neutrophils were largely enriched in the blood and BM, the source for virtually every functional study on neutrophils to date. We therefore expect that analyses of neutrophils in other tissues will uncover new functions for organ homeostasis, a notion that we assimilate to the division of tasks between monocytes for immune-surveillance, and resident macrophages for the support of organ homeostasis (Ginhoux and Guilliams, 2016; Wynn et al., 2013).

A relevant, distinctive feature of neutrophils, when compared with other tissue-resident immune populations, is their short lifespan. Estimation of neutrophil lifetimes in mice and humans have been restricted to the BM and blood, in part due to the general perception that entry into tissues implied rapid elimination (Hidalgo et al., 2019). We show, however, that their lifetimes in tissues equal or even exceed those in blood, a finding that suggested that, while transient, it was plausible for neutrophils to acquire new properties and functions within tissues. Their short lifespan is also relevant in light of the periodic (i.e., circadian) production and clearance of neutrophils into tissues (Casanova-Acebes et al., 2018), a property of neutrophils that suggests that their influence in tissues may follow circadian patterns. In other words, it is conceivable that neutrophils specialize in instructing temporal cues for tissue physiology, as illustrated in the BM where infiltrating neutrophils induce the circadian release of hematopoietic stem cells to the circulation (Casanova-Acebes et al., 2013). Therefore, a logical extension of our studies will be to explore the circadian properties of tissues that are under the control of neutrophils. In addition to these circadian considerations, the generation and use of the iLy6G^{tdTom} mice to track neutrophil lifetimes should prove useful to estimate how pathological states, aging or additional tissue environments affect the lifetime of neutrophils. This is of particular interest given the prominent pathogenic roles of these cells in the context of vascular inflammation and cancer (Nicolas-Avila et al., 2017).

An outstanding question is how neutrophils acquire their tissue-associated properties. For macrophages, this has been shown to be the result of the coordination between master regulators like PU.1 and different transcription factors to elicit transcriptional programs in a tissue-specific manner (Lavin et al., 2017; Natoli and Ostuni, 2019). It is possible that neutrophils resort to similar regulatory networks that are ultimately activated

by local cues to enable regional gene transcription (Ng et al., 2019), as hinted from our ATAC-seq analyses. In this regard, the reduced lifespan of neutrophils should not represent a limitation given that monocytes (or even macrophages) have also been shown to be rapidly re-programmed, when niches become available, to acquire transcriptional features of resident macrophages (Bonnardel et al., 2019). Interestingly, in the case of lung neutrophils we find specific areas enriched in the chemokine CXCL12 and dependence on its receptor, CXCR4, that suggest the existence of similar instructing regions, or niches, where neutrophils receive the signals needed for re-programming. This phenomenon may be important to define the number of neutrophils that can populate a given tissue, and their correct migration to areas where they can receive local signals, as illustrated by the distinct distribution of intestinal neutrophils around ILFs. Whether other bona fide niches for neutrophils exist in other organs, if tissue-to-tissue differences exist, or how this can be altered in pathological states represent important goals for future studies.

Finally, we identify neutrophils with angiogenic properties in the lung and the intestine. Similar pro-vascularizing features have been reported in the context of ischemia and hypoxia, liver injury, and irradiation (Bowers et al., 2018; Christoffersson et al., 2012; Wang et al., 2017), and are believed to facilitate vascular repair through secretion of cytokines, metalloproteases or by phagocytosis of cellular debris. An intriguing possibility is that these angiogenic neutrophils may be recruited from preexisting populations in these tissues. Studies aimed at identifying and specifically disrupting the pathways involved in the angiogenic programming will be needed to solve this question, and will be relevant to identify new therapeutic targets in pathological angiogenesis.

In summary, the appreciation that adaptation to tissues is a general property of myeloid leukocytes (at least macrophages and neutrophils, but possibly other subsets as well (Cohen et al., 2018; Gentek et al., 2018)) reinforces the concept of innate immunity as a *bona fide* functional component of tissues. This notion should incite exploration of the mechanisms that mediate myeloid adaptation to tissues, as they may be important for diagnosis and therapies of diseases that involve alterations of the innate immune system.

Acknowledgments

We thank all members of our laboratories and R. Benedito for discussion and insightful ideas; the Pluripotent Cell Technology and Transgenesis Units at CNIC for the generation of mice; E. Prieto, J. M. Ligos, M. Vitón, and R. Nieto, for help with sorting and cytometric analyses; L. Cabezuela, E. Santos and R. Mota and the animal facility at CNIC for animal husbandry, animal procedures and histology; V. Labrador, E. Arza and the Microscopy Unit at CNIC for help with microscopy; J. Winterhalter for help with embryo studies; Alicia Garcia-Culebras and Marta Dueñas from the Instituto de Investigación 12 de Octubre for their help with the Nanostring platform. This study was supported by Intramural grants from the Severo Ochoa program (IGP-SO), grant from Fundació La Marató de TV3 (120/C/2015-20153032), grant SAF2015-65607-R from Ministerio de Ciencia e Innovación (MICINN) with co-funding by Fondo Europeo de Desarrollo Regional (FEDER), RTI2018-095497-B-I00 from MICINN, HR17_00527 from Fundación La Caixa, and by Transatlantic network of excellence (TNE-18CVD04) form the Leducq Foundation to A.H. I.B. is supported by fellowship MSCA-IF-EF-748381 and EMBO Short-Term Fellowship 8261. A.R-P. is supported by a fellowship (BES-2016-076635) and J.A.N. by fellowship SVP-2014-068595 from MICINN. R.O. is supported by ERC Starting Grant 759532, Italian Telethon Foundation SR-Tiget Grant Award F04, Italian MoH grant GR-201602362156, AIRC MFAG 20247, Cariplo Foundation Grant 2015-0990 and the EU Infect-ERA 126. C.S. is supported by the SFB 1123, project A07, as well as the DZHK (German Centre for Cardiovascular Research) and the BMBF (German Ministry of Education and Research) (grant 81Z0600204). L.G.Ng is supported by SIgN core funding from A*STAR. The CNIC is supported by the MICINN and the Pro-CNIC Foundation, and is a Severo Ochoa Center of Excellence (MICINN award SEV-2015-0505).

Author contribution

I.B., A.R-P., M.G., I.K., G.F., S.G., T.E.K., E.G., J.A.N-A., T.V., A.M., J.L., J.M.A, A.A-C., J.A.Q., S.M.S., F.M., S.A. performed experiments and analyses. E.L., A.R-P., T.E.K. A.B., G.B. performed bioinformatics analyses, M.G., F.G., E.N., A.D., C.R, C.S., L.G.N., R.O. contributed essential reagents. I.B., I.A.U., O.S., L.G.N., R.O. and A.H. designed and supervised experiments. A.H. and I.B. wrote the manuscript, which was edited by all authors.

Conflicts of interest statement

The authors declare no conflicts of interest

Figures and figure legends

Figure 1. Short and variable lifetimes of neutrophils in tissues

(A) Experimental scheme for the estimation of neutrophil lifetimes using parabiosis. Graphs show the dynamics of clearance of partner-derived neutrophil after separation of the parabionts. Data show the percentage of chimerism found in tissues at 1, 4, 12 and 18 days after separation, from at least 3 mice per time point. **(B)** Experimental scheme (top) and frequencies of CD11b$^+$ Ly6G$^+$ Tomato+ neutrophils in tissues of adult iLy6G^{tdTom} mice at the indicated times after tamoxifen injection, with the 95% confidence intervals shown in color for each curve together with the calculated half-lives (red numbers) in each tissue. The curves were calculated via nonlinear regression of a mathematical model for the decay kinetics of pulsed-labeled neutrophils (see Methods and Fig.S1B-E). Data are from at least 3 mice per time point. **(C)** Fate mapping of embryonic neutrophils in postnatal tissues. Tamoxifen was administered at E15.5 (see Methods) and the percentage of CD11b$^+$ Ly6G$^+$ tdTomato$^+$ neutrophils was determined in the indicated tissues in the pups at postnatal day 1 and 7. Data are representative of 3 independent litters. At least 5 pups were included in the analysis.

Figure 2. Mass cytometry and single cell RNAseq identify tissue-specific neutrophil populations

(A) tSNE plots of mass cytometric analysis of CD11b$^+$ Ly6G$^+$ neutrophils, CD11b$^+$ CD115$^+$ monocytes, SiglecF$^+$ CD11c$^+$ alveolar Macrophages, as well as skin, bone marrow and skin macrophages (defined as F4/80$^+$CD11b^{low}), CX3CR1$^+$ MHC-II$^+$ Ly6C^{NEG} intestinal macrophages, B220$^+$ B cells and CD49b$^+$ NK1.1$^+$ NK cells obtained from the bone marrow, blood, spleen, intestine, skin and lung. Clusters are color coded by cell type. **(B)** tSNE visualization from (A) highlighting macrophages (top) and neutrophils (bottom) colored by tissue of origin. **(C)** Cluster distribution (stacked colored bars) of macrophages (left) and neutrophils (right). See Fig S2C for cluster identification. **(D)** tSNE showing the distribution of neutrophil clusters as defined by the mass cytometric analysis. Each cluster is color-coded, and plots at bottom highlight cells from each individual tissue. **(E)** tSNE visualization of the single cell RNA-sequencing analysis of neutrophils, which are colored by the tissue of origin. **(F)** Expression of selected genes on the tSNE plot from the data in (E), with colors corresponding to expression levels in TP10K.

Figure 3. Transcriptional and chromatin heterogeneity in the steady state

(A) Experimental design and morphological characterization of sorted partner-derived neutrophils from parabionts (top). Heatmap at bottom show the scaled expression of the top 100 signature genes (Log_2FC) in each tissue, obtained by bulk RNA sequencing. See Table S2 for the complete list of tissue signature genes. Scale bar 10μm. **(B)** UpSet plot of differentially expressed genes in pairwise comparison for each tissue with the rest of tissues. **(C)** Tissue scores from the bulk RNA sequencing were projected on the scRNA-seq analysis from Figure 2E. See methods for details on score calculation. **(D)** Principal Component Analysis (PCA) of the differentially accessed regions obtained by ATAC-sequencing analysis. **(E)** Overlap of the differentially accessible peaks in pairwise comparison between tissues. **(F)** K-means clustering based on the Z-score of peak

accessibility at Likelihood Ratio Test (LRT). Peaks were obtained from pooled samples. See Table S2 for the complete LRT of differentially accessible peaks. **(G)** Projection of the score expression of genes from cluster 3 in (F) on the neutrophil scRNA-seq dataset, as shown by tSNE visualization from Figure 2E. **(H)** Accessibility peaks of representative gene loci in neutrophils from the indicated tissues. **(I)** Expression of CD74, CR1/2, CD14 and IL1b in tissue neutrophils as determined by flow cytometry. Data are from at least 3 mice. ***p<0.001, **p<0.01, *p<0.05 as determined by ANOVA with Tukey multiple comparison test (I).

Figure 4. Neutrophil properties are acquired in tissues

(A) tSNE of scRNA-seq from blood neutrophils showing tissue-specific signature scores (from Figure 3A). **(B)** 3D PCA of blood, spleen and lung neutrophils obtained from specific pathogen-free (SPF) or germ-free (GF) mice (left), and scaled expression of differentially expressed genes in selected tissues (right). See Table S3 for a complete list of the differentially expressed genes. **(C)** tSNE plot of mass cytometric data of neutrophils from blood, bone marrow, spleen and lung of partner-derived (top) or endogenous (bottom) cells from parabiotic pairs. **(D)** Cluster distribution of partner- and host-derived neutrophils from the data in (C). **(E)** Profile of surface markers in bone marrow neutrophils (top) transferred to lungs (middle) or spleen (bottom). Red histograms represent expression of the transferred BM neutrophils and blue histograms indicate expression in the resident lung and spleen neutrophils. Plots are representative of at least 2 independent experiments. **(F)** mRNA expression profiles of bone marrow neutrophils 18h after transfer into lungs. Bar graphs show mean normalized expression ± SEM of the indicated genes in transferred BM neutrophils, in endogenous lung neutrophils (blue), or lung neutrophils derived from the transferred bone marrow cells (green); data are from at least 4 mice. ***p<0.001, *p<0.05 as determined by ANOVA with Tukey multiple comparison test.

Figure 5. Angiogenic properties of pulmonary and intestinal neutrophils

(A) Heatmap of showing pathway analysis results, with colors indicating Z-scores of selected enriched signaling pathways in tissue neutrophils. For complete IPA analyses and differentially expressed genes see Table S4. **(B)** Venn diagram of differentially expressed genes in lung versus all other tissues (left) and scaled expression of genes upregulated in lung. Pro-angiogenic genes are indicated. **(C)** Scaled proangiogenic score in different leukocyte subsets from the scRNA-seq analysis in the analyzed tissues. For the complete list of pro-angiogenic genes see Table S5. **(D)** Z-score levels of expression of selected pro-angiogenic genes. **(E)** Endothelial cell proliferation in lungs from control and mice with induced neutropenia for 7 days (*MRP8*^{CRE}; iDTR). Dot plots indicate the percentage of dividing Ki67^{+}CD31^{+} cells in adults, 4 week-old and mice 7 days after irradiation; data are from at least 3 mice. **(F)** Endothelial cell proliferation in the colon of adult (8-10 w.o.) or 4 week-old mice with or without induced neutropenia. Dot plots indicate the percentage of dividing Ki67^{+}CD31^{+} cells; data are from at least 3 mice. **(G)** Whole-mount imaging of the colon of control or DT-induced neutropenic mice. Images show the vasculature outside (cyan) or inside (purple) isolated lymphoid follicles (ILF, shadowed in yellow / grey). Right, dot plot indicates the percentage of CD31^{+} signal inside ILF, or in the rest of the submucosal layer; Data from at least 14 ILF/submucosa areas, 4 mice per group. Scale Bar 50um. **p<0.01, *p<0.05 as determined by the Student's t-test (E and F) and by the Mann-Whitney test (G).

Figure 6. CXCR4 guides neutrophils to areas of tissue-reprogramming in the lung
(A) Gene expression profiling of blood and lung neutrophils from control mice, mice treated with blocking antibodies against GM-CSF or TGFβ, and CXCR4$^{\Delta N}$, BMAL1$^{\Delta N}$ or NR4A1$^{\Delta N}$ mice. Bar graphs show mean normalized gene expression ± SEM in the indicated genes using Nanostring technology. Data are for 3 mice per condition. **(B)** PCA of control and CXCR4$^{\Delta N}$ neutrophils from lung and blood using the complete gene set analyzed by Nanostring profiling (see Table S5). **(C)** Whole mount imaging of lung tissue, showing neutrophils (red) and CXCL12^{+} vessels (green). The small image at right shows an 3D reconstruction detail (dotted area) of neutrophils contacting CXCL12^{+} structures. The dot plot shows the mean distance to the closest CXCL12^{+} structure of neutrophils, or randomly distributed points; data from 569 neutrophils and 481 random points, from 3 mice. Scale bar 70μm, inset 10μm. **(D)** Changes in lung endothelial cell proliferation in control or CXCR4$^{\Delta N}$ mice 7 days after irradiation. Dot plots show mean fold-change values normalized to the corresponding non-irradiated group; data from at least 5 mice per group. **(E)** Vessel area inside intestinal ILF in wild type or CXCR4$^{\Delta N}$ mice. Data is from at least 23 ILFs, 4 mice per group. **(F)** Representative images of wild type and CXCR4$^{\Delta N}$ neutrophil trajectories in lung vessels, assessed by intravital microscopy. See also Movie S1. Dot plots show mean neutrophil displacement, speed and straightness from 4 mice. **(G)** Relative frequencies of wild type and CXCR4$^{\Delta N}$ neutrophils found in the lung of transplanted chimeric mice. Dot plots show the mean ratio of chimerism (lung to blood); data are from 8 mice. **(H)** Transcriptional profile of CXCR4$^{\Delta N}$ BM neutrophils 18h after intra-tracheal transfer into lungs. Bar graphs show mean mRNA normalized expression ± SEM of the selected genes from donor CXCR4^{DN} BM neutrophils, host-derived lung neutrophils, or the transferred neutrophils (green); data are from at least 4 mice. ***p<0.001; **p<0.01; * p<0.05 as determined by ANOVA with Tukey multiple comparison (A, D and H) and Student's t-test (C, E, F and G).

Supplemental Figure titles and legends

Figure S1. Lifespan and lineage tracing of neutrophils in tissues, related to Figure 1.
(A) Characterization of partner-derived neutrophils in tissues, as in Figure 1A. Plots indicate the gating strategy used to differentiate endogenous CD45^{+} Ly6G^{+} GFP^{NEG} (orange) from partner-derived CD45^{+} Ly6G^{+} GFP^{+} neutrophils (green) in the different tissues by flow cytometry. **(B)** Schematics of the Ly6G^{CreERT2}; Rosa26^{tdTomato} (iLy6G^{TdTom}) mice. An iCRE-ERT2 cassette was inserted in exon 2 of the Ly6G gene. Tamoxifen-induced recombination of the Rosa26^{tdTom} locus leads to Tomato expression in neutrophils. **(C)** Analysis of Ly6G expression in blood leukocytes from Ly6G$^{+/+}$, Ly6G$^{+/CreERT2}$ or Ly6G $^{CreERT2/CreERT2}$ by flow cytometry. **(D)** Phenotypic characterization of tdTomato^{+} cells in the bone marrow of iLy6G^{tdTom} mice 24h after tamoxifen injection (left) and percentage of tdTomato^{+} blood leukocytes among CD45^{+}CD11b^{-} lymphoid cells, CD11b^{+}Ly6G^{-} myeloid cells and CD11b^{+}Ly6G^{+} neutrophils 2 and 3 days after tamoxifen injection (right). **(E)** Mathematical modelling used to calculate the half-lives ($t_{1/2}$) and lifespans ($t_{10\%}$) of tdTomato^{+} neutrophils in tissues shown in Figure 1B. Shown at right are the statistically significant intervals determined by the model for each tissue. See Methods for details on the analysis.

Figure S2. Mass cytometric and single cell RNA-seq profiling of leukocytes in tissues, related to Figure 2.
(**A**) Heatmap depicting the scaled expression of the 39 surface markers analyzed by mass cytometric analyses in neutrophils from the different tissues, with the dominant clusters shown at right. **(B)** tSNE visualization of tissue neutrophils colored by their tissue of origin (right) and scaled expression of selected markers (left). **(C)** tSNE visualization of leukocytes, with colors showing the Phenograph-assigned cluster annotations (left) and scaled expression of lineage markers from the mass cytometric analysis (right). **(D)** tSNE plots of monocytes, B and NK cells showing the tissue of origin. Bars at bottom show cluster distribution (stacked colored bars) for each cell type. For color identification of the assigned clusters, see Fig.S2C. **(A)** tSNE visualization of CD11b-enriched leukocyte populations colored by cell type **(B)** tSNE visualization of the neutrophil subset from (A) colored by cluster. **(C)** and **(D)** Scaled expression of differentially expressed genes by cluster (C) and by tissue (D). **(E)** Projection of selected genes on the neutrophil tSNE plot with color intensity corresponding to expression levels. (**F**) tSNE plots of the scRNA-seq of total leukocytes (left) and neutrophils (right) showing the progenitor signature score. See methods for score calculation. **(G)** Expression of selected progenitor-associated genes in each neutrophil cluster. **(H)** tSNE plots of neutrophils showing the signature scores for GMP, proNeu and preNeu progenitors. **(I)** Pseudo-time analysis of neutrophil trajectories in a diffusion map, color-coded by tissue. DC, Diffusion Component.

Figure S3. Localization, chromatin and transcriptomic analyses of tissue neutrophils, related to Figure 3.
(A) Maximum intensity projection in optically cleared organs using light-sheet microscopy, showing the distribution of vessels (red) and neutrophils (green). Data is from 2–3 mice. Scale bars, 100 μm. **(B)** Micrographs of tissues from parabiotic mice illustrating the presence of partner-derived neutrophils (red) from Ly6G-Tom reporter mice in host tissues. Scale bars, 10 μm. Partner-derived neutrophils were preferentially found in extravascular areas or within vessels (intravascular), depending on the tissues, as quantified in the bar graph (left). Bars show mean ± SEM values from the analysis of 18–71 images per tissue. Data is from 3 mice. **(C)** Whole-mount staining of an ILF-surrounding area in the submucosal layer of the large intestine (left panel), or lung tissue (right panel). 3D rendered reconstructions show the intra or extravascular localization of neutrophils (green) relative to vessels (gray). Scale bars, 50 μm or 10 μm (insets). **(D)** mRNA levels of signature genes in neutrophils from blood, bone marrow and spleen (left panel), or from lung (right panels). In these experiments, neutrophil we isolated using the same treatment and protocol, including incubation with the same enzyme mix (EM). Bar graphs show mean normalized expression ± SEM; n= 4 mice. **(E)** Accessibility peaks in the indicated gene loci, corresponding to proteins found in all neutrophils subsets. Note that the chromatin peaks are steady for *S100a* genes, but vary among tissues for *Ly6g* and *Cxcr2*. **(F)** Top, enrichment of transcription factor recognition sequences in ATAC-seq peaks in Clusters 2 and 3 based on HOMER. Bottom, occurrences of PU.1 and AP-1 motifs among the different clusters**.** ***p<0.001, *p<0.05, as determined by one way ANOVA with Tukey multiple comparison test (D; left) or Student's t-test analysis (D; right).

Figure S4. Neutrophil heterogeneity is imprinted in tissues, related to Figure 4.
(A) tSNE of blood neutrophils color-coded by cluster (left) and scaled expression of selected genes from each cluster. For the complete list of differentially expressed genes (DEG) see Table S2. **(B)** Distribution of differentially expressed genes across tissues as defined by a likelihood ratio test (LRT) analysis. Note the differential pattern between "sterile" (BM, spleen and blood) and "barrier" (lung, intestine, skin) tissues. **(C)** Scaled

expression of selected DEGs between blood neutrophils from GF and SPF mice. **(D)** tSNE visualization of clusters of neutrophils from Figure 4C (top), with the clusters found in each tissue shown at bottom. **(E)** Time course expression of CD11b, IL1b, CD14, CR1/2, CD74 and CXCR2 in bone marrow neutrophils transferred to the lung (yellow) and spleen (green), 0, 3 and 16h after transfer, as determined by flow cytometry. Data are from 2-3 mice. **(F)** Time course expression of selected genes in bone marrow neutrophils transferred to the lung 0, 3 and 16h after transfer as determined by RT-PCR. Data are from at least 4 mice. **(G)** Heatmap showing the scaled expression of selected genes from neutrophils sorted from the indicated tissues, as determined by RT-PCR. **(H)** mRNA expression in bone marrow neutrophils 16h after transfer into the peritoneum. Bar graphs show mean mRNA normalized expression ± SEM of the indicated genes in donor BM neutrophils, endogenous peritoneal neutrophils, or the transferred BM neutrophils recovered from the peritoneum; data are from at least 4 mice. **(I)** tSNE plot of neutrophils from lungs of healthy and tumor-bearing mice from the Zilionis et al. (2019) dataset. **(J)** Tissue scores projected on the Zilionis et al. dataset of lung neutrophils. **(K)** tSNE and violin plots showing expression of selected signature genes from the BM, blood and lung. ***p<0.001,**p<0.01,*p<0.05 as determined by two way ANOVA (E) or one way ANOVA with Tukey multiple comparison test (F,H).

Figure S5. Hematopoiesis- and vascular-supportive functions of neutrophils in tissues, related to Figure 5.

(A) Scaled expression of selected genes associated with proliferation and differentiation from the bulk RNA-seq analysis. (**B)** Experimental design used to induce genotoxic damage in control and neutropenic mice. **(C)** Microbiological blood status in control and neutropenic mice. Shown are hemocultures from 11 control and 14 neutropenic performed 7 days after DT treatment. Red numbers indicate the number of bacteremic mice. **(D)** Effect of neutrophil depletion in the recovery of leukocyte counts after genotoxic damage in blood, bone marrow and spleen. Dot plots show the number of neutrophils, eosinophils, ly6C^{hi} and Ly6C^{lo} monocytes, B cells, T cells, NK cells and macrophages in non-irradiated or irradiated (right, gray columns) in control (black dots) or neutropenic (red dots) animals; data are from at least 5 mice. **(E)** Spleen weight was measured in the experimental groups from (D). Data are from at least 5 mice. **(F)** Representative immunohistochemical images of bone marrow and spleen stained for B220^{+} cells in control or neutropenic mice, 7 days after irradiation. **(G)** Heatmap showing scaled expression of selected angiocrine factors in tissue neutrophils, as determined by bulk RNA-sequencing. **(H)** Flow cytometric characterization of CD49d and CXCR4 expression in tissue neutrophils. Bar graph shows the percentage of CD49d^{+} neutrophils identified in tissues. Data are from at least 2 mice. **(I)** Representative immunohistochemical staining of CD31 in the lung of control and neutropenic mice, 7 days after DT treatment. Scale bar, 500μm. Inset, 50μm. **(J)** Dot plot showing the percentage of endothelial cell proliferation in the spleen and bone marrow of control and neutropenic mice at 4 weeks of age. **(K)** Representative whole mount immunofluorescence staining showing vessels and neutrophils in ILFs in the colonic submucosa from control (top) or neutropenic (bottom) animals. Scale bar, 100μm. **(L)** Representative immunohistochemical staining of lamina propia macrophages in control and neutropenic mice, 7 days after DT treatment. Scale bar, 100μm. Inset, 20μm. ***p<0.001, **p<0.01, *p<0.05; n.s., not significant, as determined by Student's t-test analysis.

Figure S6. Differential effect of *Nr4a1* and *Cxcr4* on neutrophil reprogramming in lungs, related to Figure 6.

(A) Nanostring profiling of Cre^{NEG} control or $Nr4a1^{\Delta N}$ blood and lung neutrophils. Heatmap shows the scaled expression of all transcripts used in the analysis. **(B)** Endothelial cell proliferation in lungs from control and $Nr4a1^{\Delta N}$ mice in irradiated or non-irradiated mice. Dot plots show mean fold-change values normalized to the corresponding non-irradiated group. Data are from at least 3 mice. **(C)** Representative image of lungs from $Cxcl12^{GFP}$ mice. Shown are CXCL12-expressing cells, neutrophils and vessels. Scale bar, 50 μm. **(D)** Representative 3D reconstruction of bone marrow neutrophils from $Ly6G^{Tom}$ mice transferred into lungs of $Cxcl12^{GFP}$ mice, 16h after transfer. Shown are CXCL12-expressing cells (green) and transferred neutrophils (red). The histogram (right) shows distance distribution of the transferred neutrophils to the closest $CXCL12^{+}$ vessel vs. randomly distributed points. Data are from 2 mice. Scale bar, 40μm **(E)** Representative whole-mount images of the intestinal submucosa from control or $CXCR4^{\Delta N}$ mice. Right, distribution of vessels (purple) inside ILFs. Scale bar, 50μm. **(F)** Survival curves of control and $CXCR4^{\Delta N}$ mice after influenza A infection. Data are from 6-8 mice. **(G)** Representative images of endothelial cell density in lungs from control and $CXCR4^{\Delta N}$ mice at day 0 (top) or 14 (bottom) after infection with the influenza A virus. Endothelial cells (ERG^{+}) and all nuclei (DAPI) are shown. Images are quantified in dot plot at right. Data are from 4 mice. **(H)** Number of crawling neutrophils (left) and total neutrophils (normalized to blood counts; right) per field of view, as assessed by intravital imaging of lungs from control and $CXCR4^{\Delta N}$ mice. Data are from 4 mice per group. ***p<0.001, **p<0.01, *p<0.05, n.s.; not significant, as determined by ANOVA analysis with Tukey multiple comparison test (B), Student's t-test analysis (D and G) or Log-rank analysis (F).

STAR Methods

Resource Availability

Lead Contact

Further information on materials, datasets, and protocols should be directed to and will be fulfilled by the Lead Contact, Andres Hidalgo (ahidalgo@cnic.es).

Materials Availability

This study generated the Ly6G^{CRERT2} mouse line, which is available from our laboratory through standard Material Transfer Agreement (MTA).

Data and Code Availability

All the omics data is available as a super-series in GEO under the accession number GSE143255. The individual accession numbers are as follows: Tissue leukocyte cells scRNAseq data: GSE142754. Tissue neutrophils bulk RNAseq data from parabiosis: GSE141745. Germ free and SPF tissue neutrophils bulk RNAseq data: GSE142432. Tissue neutrophils ATACseq data: GSE141285.

Experimental Model and Subject Details

Mice

All experiments were performed on 6–12-wk-old C57BL/6 male and female mice. Chow and water were available ad libitum. The following knock-in or transgenic mice were used: Cxcr4$^{flox/flox}$ (Nie et al., 2004), *hMRP8*^{CRE} (Passegue et al., 2004), *Cxcl12*^{GFP} (Sugiyama et al., 2006), Rosa26^{iDTR} (Buch et al., 2005), *Ly6g*^{CRE}; Rosa26^{tdTomato} (Hasenberg et al., 2015). Mice with neutrophil-specific deficiency in CXCR4, Bmal1 or Nr4a1 were generated by crossing hMRP8^{CRE} with Cxcr4$^{flox/flox}$ mice (Cxcr4$^{\Delta N}$ mice), Arntl$^{flox/flox}$ (Bmal1$^{\Delta N}$ mice), (kindly provided by S. Benitah; (Janich et al., 2011)) or Nr4a1$^{flox/flox}$ (Nr4a1$^{\Delta N}$ mice; floxed mice kindly provided by Gerhard Krönke). All mice were in the C57BL/6 background and were maintained on a 12h light/12h darkness schedule. Mice were housed in a specific pathogen–free facility at Fundación CNIC. Experiments exploring the effect of microbiota in neutrophil transcriptional profile were performed with mice housed in the Translational Animal Research Center (TARC) of the University Medical Center Mainz under specific-pathogen-free (SPF) or germ-free (GF) conditions in EU type II cages with two to five cage companions with standard autoclaved lab diet and water ad libitum, 22°C ± 2°C room temperature, and a 12-h light/dark cycle. All experimental procedures were approved by the local Animal Care and Ethics Committees.

Generation of iLy6G^{tdTom} mice

Ly6G^{CreERT2} mice were generated at the Transgenesis and Pluripotent Cell Technology Units of CNIC. Briefly, a creERT2 fusion gene (a Cre recombinase fused to a human estrogen receptor ligand binding domain) followed by an SV40 polyadenylation signal, and a FRT-flanked neomycin resistance (neo) cassette was inserted into the exon 2 of the *Ly6G* gene by homologous recombination in ES cells (*Ly6G*^{CreERT2}). Flp-mediated recombination removed the FRT-flanked neo cassette and knock-in mice were then backcrossed onto a C57BL/6 background for 8 generations to eliminate off-target effects. Finally, to generate an inducible reporter to track neutrophils, Ly6G^{CREERT2} mice were crossed with Rosa26^{Tdtomato} mice (Madisen et al., 2010), resulting in the iLy6G^{tdTom} mice used in our experiments. For colony genotyping, we used the following primer

sequences: 5´-ACTAACCAGCTTCGACTTCCAAGG RV (Wt), 5´-TTGGGACGGTCGCTTTGGTAG- and 5´-GGAACCTTCAGCTTCGACCAATCA (Tg). Wild type band size: 315b.p. and transgenic band size: 648bp. Alternatively, the Cre-ERT2 insertion was confirmed by flow cytometry as shown in Fig. S1.

Animal treatment

To induce neutropenia, 4 and 6-12 week-old male and female $Mrp8^{Cre}$ iDTR mice were injected intraperitoneally with 10 µg/kg of diphtheria toxin (DT; Calbiochem) for 7 days. Injections were done every 2 day. An intraperitoneal injection of tamoxifen (4mg/mice) was performed to induce CRE recombinase activity in 6-12 week-old male $iLy6G^{tdTom}$ mice. Maximum pulse labelling efficiency was reached 3 days after tamoxifen administration in blood and in tissues, and affects 5-10% of the overall neutrophil population. To explore the role of GM-CSF and TGFβ in neutrophil tissue specification by Nanostring profiling, 6-12 week-old C57BL/6 male mice were treated i.v. with 100 µg of anti-GM-CSF (BE0259 BioxCell, MP1/22E9) or anti-TGFβ (BE0057 BioxCell 1D/11) antibodies for 3 consecutive days before harvest. To study the role of neutrophils on endothelial cell proliferation and on leukocyte counts recovery, 6-12 week-old male and female mice received a 6Gy irradiation dose and measurements were made 7 days after irradiation.

Parabiosis

We followed previously published procedures (Casanova-Acebes et al., 2018). Briefly, anesthetized 6 week-old male mice were shaved and matched incisions were made from the olecranon to the knee joint, then olecranon and knee were attached by a single suture from one mouse to the other, using 5-0 polypropylene, and the dorsal and ventral skins were stitched by continuous suture. Analyses were done 4 weeks after surgery.

Generation of Transplant Chimeras

To address the competitive advantage of wild type vs. $CXCR4^{\Delta N}$ neutrophils in the lungs, we generated mixed bone marrow chimeras. Donor BM cells were harvested from CD45.1 or $MRP8^{CRE+}$ $Cxcr4^{f/f}$ 6-12 week-old males by flushing the femur with PBS. Recipient wild-type C57BL/6 6-12 week-old male mice were lethally irradiated (two 6Gy doses, 3 h apart) before receiving 1 million BM nucleated cells by intravenous injection. For mixed chimeras, equal numbers of experimental CD45.2 and wild-type CD45.1 BM cells were mixed before intravenous injection. Engraftment of recipient animals was assessed 8–10 weeks after transplantation by analysis of the percentage of mutant and CD45.1 leukocytes in blood by flow cytometry.

Method details

Preparation of single cell suspensions from tissues

Blood was taken through cardiac puncture with 1ml syringe attached to a 26g needle filled with 50µL of 0.5M EDTA. Samples were lysed in RBC lysis buffer (eBioscience) for 4min. For BM cells, mice femurs were flushed using a 23–gauge needle in PBS containing 2mM EDTA and 2% fetal bovine serum (FBS) and passed through a 70–µm nylon mesh sieve. Spleens were harvested and homogenized into single-cell suspensions using 70–µm nylon mesh sieves and syringe plungers. Lungs and ear skins (dorsal and ventral side separately) were harvested and cut dry into small pieces before digested in liberase TM (Roche) and DNase1 (Sigma) for 45min at 37˚C. Lung and skins were then homogenized into single-cell suspensions using 70–µm nylon mesh sieves and syringe plungers. Colons were harvested and cleaned of fecal matter before cutting longitudinally. Colons were washed in cold PBS to remove fecal contents and then shaken once in 20ml of cold PBS in a falcon tube. Colons were then incubated in 100mM EDTA for 30 min at 37˚C in shaking incubator (250rpm). Tubes were shaken once to

remove epithelial cells. Colons were cut into pieces and digested in 6-well plates containing liberase TM and DNase1 for 30min at 37˚C. Colons were then homogenized into single-cell suspensions using 70–μm nylon mesh sieves and syringe plungers.

Mass cytometry

Preparation of tissues for cyTOF analysis

Single cell suspensions from blood, bone marrow, spleen, lung, intestine and skin from 6-12 week-old male mice were subjected to CD45 MACSbeads positive selection (Miltenyi Biotech) according to the manufacturer's instructions. After selection, samples were plated in a 96-well round bottom plate at a density of 5 x 10^6 cells per well. Cells were stained for viability with 100μL of 50μM of cisplatin (Sigma-Aldrich) for 5 minutes at 4°C. Cells were then washed with staining buffer (4% FBS, 0.05% sodium azide, 2mM EDTA in PBS) and incubated with anti-CCR2-APC, anti-CD34-FITC, anti-CD115-PE and anti-Flt3-biotin in 50μL reaction volume for 90 minutes at 4°C. Red blood cells were lysed with RBS lysis buffer (eBioscience) and cells were washed with staining buffer. Cells were stained with 50μL of metal isotope-labeled surface antibodies on ice. After 30 minutes, cells were washed twice with staining buffer, once with PBS, and then fixed in 2% paraformaldehyde (PFA) (Electron Microscopy Sciences) in PBS at 4°C overnight. The next day, cells were pelleted and re-suspended in 200μL permeabilization buffer (Biolegend) and allowed to stand for 5 minutes on ice. Cells were then washed once with PBS and incubated with cellular barcodes on ice for 30 minutes. Subsequently, cells were washed once with perm buffer and in staining buffer for 10 minutes on ice. Cellular DNA was labeled at room temperature with 250nM iridium intercalator (Fluidigm) in 2% PFA/PBS. After 20 minutes, cells were washed twice with staining buffer.

Prior to acquisition, cells were washed twice with water before final re-suspension in water. Cells were pooled from all samples, enumerated, filtered and diluted to a final concentration of 0.6 x 10^6 cells/mL. Mass-tag barcoding was used so that all samples could be acquired simultaneously. EQ Four Element Calibration Beads (Fluidigm) were added to the pooled samples at a final concentration of 1% prior to acquisition. Samples were acquired on a CyTOF2 (Fluidigm) equipped with a Super Sampler fluidic system (Victorian Airship & Scientific Apparatus LLC) at an event rate of <500 events per second. After mass cytometry acquisition, data were exported in flow-cytometry (FCS) format, normalized and events with parameters having zero values were randomized using a uniform distribution of values between minus-one and zero.

CyTOF Analysis

For subsets identification, FSC files were analyzed with version 1.10.4 of the "cytofkit" R package. Briefly, manual gating of $CD11b^+$ $Ly6G^+$ neutrophils, $F4/80^+$ $CD11b^+$, $SiglecF^+$ $CD11C^+$ and $CX3CR1^+$ $MHC\text{-}II^+$ $Ly6C^-$ macrophages, $CD115^+$ $CD11b^+$ monocytes, $B220^+$ B cells and $CD49d^+$ $NK1.1^+$ NK cells from two independent replicates was performed using Flowjo software (Flowjo, LLC). Gated populations were merged, exported and analyzed with Phenograph (Cytofkit R package) with the following settings: merge: ceil, transformation: cytofAsinh, cluster: RPhenograph, visualization: t-SNE. 2-dimensional t-SNE maps were visualized and colored according to their cluster ID, the expression of lineage markers, or their corresponding tissue of origin.

Single cell RNA sequencing (scRNA-seq)

Library construction with 10x Genomics platform

cDNA Droplet-based digital 3′ end scRNA-seq was performed on a Chromium Single-Cell Controller (10 × Genomics, Pleasanton, CA) using the Chromium Single Cell 3′ Reagent Kit v2 according to the manufacturer's instructions. Briefly, blood, bone marrow, spleen and lung $CD45^+$ $CD11b^+$ leukocyte suspensions from 6-12 week-old C57BL/6 male mice were FACS sorted in an Aria II sorter (BD). Cells were partitioned in Gel Beads in Emulsion (GEMs) and lysed, followed by RNA barcoding, reverse transcription and PCR amplification (12–14 cycles). Sequencing-ready scRNA-seq were prepared

according to the manufacturer's instructions, checked and quantified on TapeStation 2200 (Agilent Genomics, Santa Clara, CA) and Qubit 3.0 (Invitrogen, Carlsbad, CA) instruments. Sequencing was performed on a NextSeq 500 machine (Illumina, San Diego, CA) using the NextSeq 500/550 High Output v2 kit (75 cycles), at the Center for Omics Sciences at the IRCCS Ospedale San Raffaele (COSR).

scRNA-seq processing and analysis

Reads for the single cell experiments were generated on NextSeq 500 (illumina) instrument following manufacturer recommendations. Fastq.gz files were generated from raw Illumina BCL files using 10X Genomics Cell Ranger version 2.1.1 with default parameters. The quality of sequencing reads was evaluated using FastQC v0.11.5 and MultiQC v1.5. Cell Ranger v2.1.1 was then used to align the sequencing reads to the mm10 mouse transcriptome and to quantify the expression of transcripts in each cell. UMI and cell barcodes were then filtered as described in ref. Only confidently mapped reads, non-PCR duplicates, with valid barcodes and UMIs were retained to compute a gene expression matrix containing the number of UMI for every cell and gene. All downstream analyses were implemented using R v3.6.1 and the package Seurat v3.1.1 (Butler et al., 2018; Stuart et al., 2019). For each sample, cells expressing less than 300 unique genes and genes expressed in less than 3 cells were discarded. Raw counts were then merged (resulting in 15,636 genes per 27,939 cells) and normalized using the Seurat function SCTransform after removing cells having more than 4% mitochondrial genes. The input gene expression matrix for the normalization was composed by 15,636 genes and 26,271 cells. During the normalization, the confounding sources of variation i.e. the mitochondrial mapping percentage, the S and G2M scores and the difference between them were removed. Cell cycle scores were calculated using CellCycleScoring function. The number of variable features in the SCTransform function after ranking by residual variance was set to 1000. During the normalization, 819 genes were automatically removed because expressed in less than 3 cells independently from the overall counts leading to retain 14,817 total genes. Expression data were than scaled using ScaleData function regressing on S and G2M scores. Graph-based clustering: most variable genes across the merged dataset (i.e. the highly variable genes) were identified based on the highest standardized variance. The procedure is implemented in the FindVariableFeatures function with method = "vst". A total number of 1000 genes was selected as top variable features and used to perform the PCA dimensionality reduction. A KNN graph based on the euclidean distance in the 50 PCs space was constructed using the FindNeighbors function.

Gene signatures for different cell type populations: Cells were classified according to gene signatures derived from published RNA-Seq analyses of myeloid cells. Briefly, we downloaded expression data from Immgen RNA-Seq dataset (https://www.immgen.org/). For each cell type (Neutrophils, Dendritic cells, NK cells, T cells and B cells) we extracted genes being differential in all pairwise comparisons with other cell types using glmFit and glmLRT functions from edgeR R package as described above. For each comparison, genes were called significant at FDR < $1e^{-4}$ and the top 200 ranked for decreasing fold change were selected. The final gene signature defining each cell type was the intersection of the resulting 4 lists. As monocytes were not included in Immgen dataset, we downloaded monocytes data from (Mildner et al., 2017) and calculated DEGs with edgeR (Robinson et al., 2010) as above. We retained the top 5 genes, ranked by decreasing fold change, defining classical and non-classical Monocytes. Macrophages included in Immgen dataset were from peritoneal cavity, hence we used signature defined in (Lavin et al., 2017) for macrophages from spleen. Once classified, we isolated the cells classified as neutrophils and performed a new normalization, scaling and clustering with a resolution of 0.1, using the shared nearest neighbor (SNN) method implemented in Seurat, and also a new tSNE. We performed differential expression analysis based on both the obtained clusters and the tissues. We also downloaded and analyzed data from (Zilionis et al., 2019). We isolated neutrophils

from healthy and tumoral lung tissue. We processed the reads with the standard normalization pipeline from Seurat and performed a clustering with 0.5 resolution.
For all differential expression analyses, only the genes detected in a minimum percentage of 25% of the cells in either of the two populations were reported and the testing was limited to genes which showed, on average, at least 0.25-fold difference (log-scale) between the two groups of cells. The tissue scores for each cell in the single cell dataset were obtained from the tissue signatures from the bulk RNA-seq data.
To mark progenitor cells, we created a signature made of genes from four different studies. As these studies used different nomenclatures for their neutrophil progenitor populations, we chose genes associated with early stages in each. We selected the GMP, proNeu and preNeu genes from (Evrard et al., 2018; Kwok et al., 2020); the Early and late-stage progenitor genes from (Zhu et al., 2018) and the Neu progenitor genes from (Kim et al., 2017). For the pro-angiogenic score, we downloaded all the genes annotated under the "Angiogenesis" GO category keeping for the signature only those with experimental evidence or high throughput evidence and discarding the genes related to "negative regulation". Gene are listed in Table S5.
All the scores are calculated dividing the total amount of transcripts belonging to genes from a particular signature by the total transcripts of the cell and by the number of genes in the signature. The diffusion map was obtained with the Seurat suite with 1000 nearest neighbors.

ATAC-sequencing
Blood, lung and spleen neutrophils from 6-12 week-old C57BL/6 male mice were FACS sorted using CD45, CD11b, Ly6G and DAPI labelling. For the bone marrow, $Ly6G^{+}$ $CXCR2^{hi}$ mature neutrophils were sorted. All sorted samples had with typical purities > 95%. Cell processing for ATAC-seq was performed as previously described (Buenrostro et al., 2013). Briefly, Samples were size selected using AMPure XP beads (Beckman-Coulter) to yield libraries ranging from 100 bp – 1000 bp Samples were quality checked for nucleosomal phasing and size distribution using DNA hi-sensitivity Bioanalyzer assay (Agilent). Quantification was performed with KAPA Library Quantification Kit (Illumina) and samples were pooled at an equimolar ratio and sequenced on a HiSeq2500 using 75 bp paired-end chemistry in Welcome Centre for Human Genetics, Oxford. Raw sequencing reads were trimmed with Cutadapt prior to mapping to the mm10 version of the mouse genome using Bowtie2 with the following parameters --local --X 2000. PCR duplicates were removed with PicardTools, additionally, reads mapping to chrM, with MAPQ < 10, and insert sizes >150 bp were removed prior to peakcalling. Peaks were called with MACS2 with the following settings: --format BAMPE --nomodel --keep-dup all --mfold 5 50. Peaks found in at least 2 biological replicates were kept for further analysis and merged peakset consisting on all discovered peaks was used for differential accessibility testing. Reads were counted over the merged peakset using BedTools and tested using DESeq2. Significantly differentially accessible peaks were deemed as having adjusted p-values < 0.05 (LRT test), and adjusted p-values < 0.05, and fold change > 1.5 (Wald test). DeepTools was used to generate normalised BigWigs from all biological replicates, which were merged for visualisation**.** *De novo* motif discovery was performed using Homer findMotifs.pl on the central 100 bp from all of the peaks in each cluster using a local background comprising the 100 bp flanking sequences of each peak and default settings. Motif scanning was conducted using Homer annotatePeaks.pl on 1 kb windows centered over ATAC peaks with a bin size of 5b.p. using discovered motifs.

Bulk RNA-Sequencing
Library preparation
Blood and tissue neutrophils from 10-12 week-old male mice set in parabiosis for 4 weeks were FACS sorted using CD45, CD11b, Ly6G and DAPI labelling, with typical purities >95%. cDNA amplification from neutrophil RNA and generation of index-tagged

sequencing libraries were carried out using the Ovation Single Cell RNA-Seq System (NuGEN Technologies, San Carlos CA). Libraries were quantified using the dsDNA HS assay with the Qubit fluorometer (Life Technologies, Carlsbad, California). Average library size and size distribution were determined using a High Sensitivity DNA assay in an Agilent 2100 Bioanalyzer (Agilent Technologies, Santa Clara CA). Libraries were normalized to 10nM using Tris-Cl 10mM, pH8.5 with 0.1% Tween 20. Libraries were applied to an Illumina flow cell for cluster generation (True Seq SR Cluster Kit V2 cBot) and 61 nt long, single-end reads were generated on a Genome Analyzer IIx, using the TruSeq SBS Kit v5 (Illumina) and following the standard RNA sequencing protocol. Data from the germ-free experiment were paired end sequenced in the HiSeq2500 (Illumina). The RNA sequencing experiments were performed at the Genomics Unit at CNIC.

RNA sequencing analysis

FastQ files for each sample were obtained using the CASAVA package (Illumina) to demultiplex reads according to adapter indexes and to produce fastq files. Read quality was determined with the application FastQC v0.11.5 (Schageman et al., 2013) and MultiQC v1.5. For data analysis, sequencing adaptor contaminations were removed from reads using Cutadapt v1.7.1 and the resulting reads were mapped on the transcriptome (GRCm38 Ensembl gene-build 84, without miRNAs or pseudo-genes) and quantified using RSEM v1.2.20 (Li and Dewey, 2011) and kallisto v0.43.1 (Bray et al., 2016). Genes not detected in any of the samples were not considered for statistical analysis. The R package limma v3.32.2 (Ritchie et al., 2015) was used to normalize the estimated counts from RSEM and to test differential expression using limma's moderated t test. The R package sleuth v0.3.0 (Pimentel et al., 2017) was used to normalize the pseudo-counts from kallisto and to perform the Likelihood Ratio Test across different tissues. Only genes with over 5 estimated TPMs in at least 47% of the samples were considered in sleuth. Raw and Benjamini-Hochberg adjusted p-values (FDR) were calculated for each of the tests. An adjusted p value of less than 0.05 was considered statistically significant.
The signature gens were obtained by performing several filtering steps. First, a contrast of each tissue against the rest was performed. Then, we selected the differentially expressed genes with a log2FC>2 in the tissue. Finally, the remaining genes that were upregulated only in one of the tissues but not the rest were selected for the signature.

RNA Isolation, Reverse Transcription, and RT-PCR

Total RNA was prepared with the RNA Extraction RNeasy Plus Mini-kit (QIAGEN) and RNA was reverse-transcribed with the High-Capacity cDNA Reverse Transcription kit (Applied Biosystems; Carlsbad, CA) according to the manufacturer's protocol. Real-time quantitative PCR (SYBR-green, Applied Biosystems) assays were performed with an Applied Biosystems 7900HT Fast Real-Time PCR System sequencer detector. Expression was normalized to the expression of the *36b4* housekeeping gene. Primer sequences are as follow: *36b4*: F 5'-ACTGGTCTAGGACCCGAGAAG-, R 5'-TCCCACCTTGTCTCCAGTCT-; *Ptgs2*: F 5' -TGAGCAACTATTCCAAACCAGC-, R 5'-GCACGTAGTCTTCGATCACTATC-; *Nr4a1*: F 5'- TTGAGTTCGGCAAGCCTACC-, R 5'- GTGTACCCGTCCATGAAGGTG-; *Il1b*: F 5'-AGTGAGGAGAATGACCTGTTC-, R 5'-CGAGATGCTGCTGTGAGATT-; *Tnfaip3*: F 5'-GAACAGCGATCAGGCCAGG-, R 5'-GGACAGTTGGGTGTCTCACATT-; *Cebpe*: F 5 -'GCAGCCACTTGAGTTCT CAGG-, R 5'-GATGTAGGCGGAGAGGTCGAT-;*Ltf*: F 5'-TGAGGCCCTTGGACTCTGT-, R 5'-ACCCACTTTTCTCATCTCGTTC-; *Ifitm3:* 5'-TTCTGCTGCCTGGGCTTCATAG-, R 5'-ACCAAGGTGCTGATGTTCAGGC-; *Cr2:* F 5'-TTGCTGCCAAAGTATTCTTTTGC-, R 5'-TGGAGGTTTCTAAGCAGGTGATA-; *Cd74* F 5'-AGATGCGGATGGCTACTCC-, R 5'-TCATGTTGCCGCCGTACTTGGTAAC-.

NanoString
RNA was extracted from sorted neutrophils from the blood and lung from 6-12 week-old male mice using RNeasy Mini Kit (Qiagen) and stored at -80C. Samples were subjected to the NanoString nCounter™ gene expression assay according to the manufacturer's protocol (NanoString Technologies, Seattle, WA). For the analysis, a custom nCounter® assay for quantitative assessment of expression of 48 gene element was designed (See Table S5). Raw data were analyzed by nSolver™ software (NanoString Technologies, Seattle, WA, USA) using standard settings and were normalized against the housekeeping genes.

Flow cytometry
Flow cytometry was performed at the Cellomics Unit of Fundación CNIC. Samples were acquired in a LSRII Fortessa or FACS Canto analyzer (BD Biosciences). Doublets and $DAPI^+$ cells were excluded from analyses using the FlowJo software (Flowjo LLC). To determine proliferation, cells were stained with anti-CD45 conjugated with PerCP/Cy5.5 and anti-CD31-PECy7 and then fixed and permeabilized using the Fix/Perm and Perm Buffers (eBiosciences) according to manufacturer's instructions. Cells were then stained for 30 minutes at 4ºC with an anti-mouse and rat Ki67 antibody labelled with eFluor660 and analyzed by flow cytometry. The same procedure was performed to determine IL1β levels in tissue and circulating neutrophils. Truecount beads (BD) were used to estimate leukocyte counts after genotoxic damage on single cell suspensions from blood, bone marrow and spleen. Antibodies used are listed in the key resource table.

Intravital imaging of the lung
Intravital microscopy of the lung was performed as reported (Adrover et al., 2020). Briefly, 6-12 week-old male mice were anesthetized and mechanically ventilated through the trachea using a small animal ventilator model 687 (Harvard Apparatus). Then, right lateral thoracotomy was applied, and the lung was positioned under the window of a custom-built fixation device. A mild vacuum was applied to hold the lung in position during microscopy. Mice were injected with AF647-conjugated Ly6G antibody to stain neutrophils. 4D imaging was performed for each mouse in 5 random fields inside the visualization window, using the VIVO system. Quantification of the kinetic parameters of intravascular crawling neutrophils was performed using automated cell tracking with Imaris (Bitplane AG, Switzerland).

Whole mount immunostaining and tissue clearing
4 or 6-12 week-old male and female mice were perfused with 20ml of saline through the left ventricle of the heart, and the lungs and colons were collected in cold PBS. For colon whole-mount, large intestine colons were excised and flushed with cold PBS and opened by the mesenteric border. Colons exposing the lumen upwards were placed in HBSS with 5 mM EDTA in agitation for 30 min at 37°C. Epithelial cells were removed by several washes of the intestinal surface with HBSS/EDTA. Tissues were washed in cold PBS and fixed in PFA 4% at 4°C overnight. Fixed intestines and lungs were permeabilized in methanol gradients in PBS for 30 min (PBS > MetOH 50% > MetOH 80% > MetOH 100%) and then were rehydrated through descending methanol gradients in PBS (MetOH 80% > MetOH 50% > PBS). Rehydrated tissues were washed three times in PBS containing 0.5% Triton-X 100 (PBST) and blocked overnight with PBST with 25% FBS at 4°C with shaking. Staining of neutrophils was performed with a biotinylated anti-Mrp14 antibody (clone 2B10, Abcam) or with biotinylated anti-MPO (R&D Systems) and vessels with an anti-CD31 (BD Biosciences) in 25% FBS-PBST 48h at 4°C with shaking. GFP detection was performed using a chicken anti-GFP primary antibody (Invitrogen). Tissues were washed and incubated with secondary antibodies (goat anti-rat Alexa Fluor 568 and goat anti-Armenian hamster 647; and goat anti-chicken Alexa Fluor 488 Life Technologies) and DAPI in 25% FBS-PBST over night at 4C. 48h after incubation tissues were washed for 24h in washing buffer and were dehydrated in MetOH gradients in dH20

using glass containers for 30 min in each step (MetOH 50% > MetOH 70% > MetOH 90% > three times MetOH 100%). Finally, tissues were cleared for 30 min in MetOH with 50% benzyl alcohol, benzyl benzoate (BABB) and afterwards in 100% BABB (1:2). In addition to BABB staining, lung whole mount immunostaining in CXCL12^{GFP} mice was performed using QUBIC (Susaki et al., 2014). Briefly, an anti-VE Cadherin-APC (Biolegend) and an anti-Ly6G-PE (Biolegend) were retroorbitally injected to CXCL12^{GFP} mice. 10 minutes after injection, mice were perfused with 20ml of PBS and lungs fixed for 4h with 4% PFA. Lungs were then incubated at 37C for 3 days in QUBIC1 solution. Imaging of whole-mount was performed at the Microscopy & Dynamic Imaging Unit of the CNIC using a Zeiss 780 confocal microscopy system. Additionally, organs cleared to determine neutrophil distribution in tissues were imaged using the light sheet Ultramicroscope (LaVision BioTec GmbH, Bielefeld, Germany) in BABB with 2x/0.5 objective (with zoom factor of 2.0), using a white light supercontinuum laser. Analysis and 3D-redered reconstructions were performed with Imaris (Bitplane AG, Switzerland).

Histology

4 or 6-12 week-old male and female mice were sacrificed with CO_2 and perfused with a saline solution in order to collect the tissues into a 2% PFA solution. After 24 hours in fixation solution at 4ºC, samples were cryopreserved with a sucrose gradient. For immunofluorescence staining, tissues were frozen in OCT Compound (Tissue Tek) using dry ice, cut in 12µm sections in a cryostat (Leica CM1850), block with 5% of Normal Goat Serum (Vector) for 1h at RT. To characterize the lung endothelium, tissues were stained with rabbit anti-ERG (Abcam) overnight followed by incubation with secondary goat-anti rabbit Alexa 546 antibody and DAPI. To identify neutrophil distribution, tissues were stained with anti-CD31 antibody (Abcam), followed by incubation with secondary goat-anti rabbit Alexa 488 or 647 antibody and DAPI. Endogenous tomato or GFP signal from Ly6G *Ly6g*^{CRE}; Rosa26^{tdTomato} or *Lyz2*^{GFP} mice was used to identify partner deriver or transferred neutrophils.

For immunohistochemical analysis on paraffin, sections were dehydrated and paraffin wax embedded. 4-micron sections were deparafinized and brought to TBS buffer. Antigen unmasking was performed using heat induced epitope retrieval (HIER) with Citrate buffer at pH6 (anti-B220, BD and anti-F4/80, Abcam) or Tris-EDTA buffer at pH9 (anti-CD31, Abcam). Endogenous peroxidase was blocked by incubation with H_2O_2 for 5 minutes and endogenous antigens blocked with fetal bovine serum FBS) for anti-CD31 and anti-F4/80 or bovine serum albumin (BSA) for anti-B220 during 20 minutes to subsequently incubate with the primary antibodies. As secondary antibodies, we used a HRP-conjugated rabbit anti-rat antibody (Dako P045001) for anti-B220 and F4/80 and a HRP-conjugated goat anti-rabbit polymer (EnVision® K4003, Dako) for CD31. DAB (3,3´- diaminobenzidine) was used for visualization and nuclei were counterstained with Hematoxylin. For standard Hematoxylin and Eosin staining sample were rehydrated in decreased concentrations of ethanol, then 3 min in Harris Hematoxylin, 3 seconds in Acid Alcohol and 5 min in alcoholic eosin 5% solution, dehydrate again and mount with DPX. All the immunohistochemical procedures were performed using an automated autostainer (Autostainer Plus®, Dako). For image analysis the samples were digitalized with a scanner (NanoZoomer-2.0RS, Hamamatsu).

Giemsa staining of neutrophils.

Cytologic examination of FACS-sorted neutrophils from 6-12 week-old male and female mice was performed on cytospin preparations stained with Giemsa (Sigma). Sections were examined with a FSX100 microscope (Olympus).

Influenza A infection

Influenza A virus strain A/PR8/34 (H1N1) stock suspension was diluted, and 60 PFU were administered intra-nasally to isoflurane-anesthetized 8-12 week-old male mice in

50 µl of PBS. Mouse weight was monitored daily after infection and mice that presented weight loss <20% of their initial body weight were sacrificed and considered deceased.

Adoptive transfers

TdTomato$^+$ cells from the bone marrow of Ly6G^{CRE+}Rosa26^{TdTomato} Catchup 8-12 week-old male mice were FACS sorted and resuspended in calcium- and magnesium-free PBS at a concentration of 2x10^4 cells/µl. One million (1×10^6) cells were injected intratracheally, intrasplenic or intraperitoneally to CD45.1 8-12 week-old male mice in 50µl of sterile PBS. 18h later, mice were sacrificed and lungs, spleen and peritoneal suspensions were prepared for FACS sorting. For RT-PCR analysis, 50.000 CD45.2$^+$ CD11b$^+$ Ly6G$^+$ Tdtomato$^+$ or CD45.1$^+$ CD11b$^+$ Ly6G$^+$ Tdtomato^{NEG} cells were sorted, pelleted and resuspended in 350 µl of RLT lysis buffer (Quiagen) for RNA extraction.

Mathematical modeling

To determine neutrophil half-lives and mean lifespans in tissues we used the normalized to maximum percentage of tdTomato$^+$ neutrophils (n_{Tom}) observed in blood and tissues during 1-7 days (t_j) after tamoxifen injection in adult iLy6G^{tdTom} reporter mice. In the present context, half-lives represent the time required for neutrophils to reduce their numbers to half of their values with respect to a reference time defined below. Moreover, mean lifespans account for the most long-lived 10 percent of a given cohort of neutrophils. To find the half-lives $t_{1/2}^{(i)}$ in a tissue i, we calculated the mean lifetimes τ_i and then applied the relation $t_{1/2}^{(i)} = \log(2)\tau_i$.

A first estimation of the mean lifetimes was performed by resorting to the survival function $s_i(a)$ for a cohort of pulse-labeled neutrophils after tamoxifen administration. Here, $s_i(a)$ provides the proportion of the initial cohort of tdTomato$^+$ neutrophils in tissue i that are still alive when their age is $a \geq 0$. It is a monotonically non-increasing function satisfying $s_i(a_0) = 1$, with a_0 denoting an initial reference age, and $s_i(a_{\max}) = 0$ for a sufficiently long age $a_{\max}$. The corresponding mean lifetimes in all the sampled tissues can be computed via the integral (i.e. the area under $s_i(a)$)

$$\tau_i = \int_{a_0}^{a_{\max}} s_i(a)\, da\,.$$

We set our initial reference age $a_0 = 2$ days in the case of bone marrow and $a_0 = 3$ days in all other tissues (i.e. when the normalized to maximum percentage of tdTomato$^+$ neutrophils reached 100%), both after tamoxifen injection. Moreover, $a_{\max} = 7$ days which was the last day of tissue sample collection. The survival functions for each of the tissues were constructed via cubic spline interpolation of the datasets from a_0 up to $a_{\max}$. From the obtained mean lifetimes, the corresponding half-lives that resulted were: Bone marrow (22.9 hours), blood (12.2 hours), spleen (12.8 hours), lung (11.3 hours), liver (12.1 hours), intestine (13.0 hours), and skin (21.0 hours).

As a second method to estimate half-lives and to further calculate the 95% confidence intervals displayed in Fig. S1E, we put forward a simple mathematical model comprising unlabeled and labeled neutrophils in each compartment (tissue). Our goal was to obtain closed-form formulas for the kinetics of the labeled neutrophil subpopulations suitable, at a later computational stage, for nonlinear regression analyses. To this end, let $U(t)$ and $L(t)$ denote the number of unlabeled and labeled post-mitotic neutrophils in the bone marrow (BM) at time $t \geq 0$, respectively. The ordinary differential equations (ODEs) governing the kinetics of these two subpopulations are

$$\frac{dU}{dt} = \phi - r(t)U - \frac{U}{\tau_{\mathrm{BM}}},$$
$$\frac{dL}{dt} = r(t)U - \frac{L}{\tau_{\mathrm{BM}}},$$

where ϕ represents the net flux of post-mitotic neutrophils, $r(t)$ is the labeling efficiency rate (i.e. the fraction of those neutrophils that become labeled per unit time) and τ_{BM} is the neutrophil mean lifetime in BM. For simplicity, we ignored the fact that ϕ may exhibit circadian oscillations and thus was assumed to be constant. In addition, we neglected possible repopulation from labeled neutrophils coming from the blood or other tissues into the BM. Thus, the total neutrophil population $U(t) + L(t) = N$ was regarded as constant under homeostatic conditions. The above ODE system can be solved exactly in terms of quadratures once the initial conditions are specified (i.e, $U(0) = N$ and $L(0) = 0$).

In our experiments the labeling efficiency rate $r(t)$ peaked 32 hours after tamoxifen injection and had a localized time profile with a full width at half maximum of about 21 hours. Thus, once $r(t)$ becomes sufficiently small, the temporal dependence of $L(t) \propto e^{-t/\tau_{\mathrm{BM}}}$.

We next considered the kinetics of the labeled neutrophils originating from the BM and subsequently released into the circulation and other tissues. Let $L_i(t)$ denote the corresponding number of labeled neutrophil subpopulation in compartment i at time $t \geq 0$. The ODEs governing the kinetics of these subpopulations are

$$\frac{dL_{\mathrm{i}}}{dt} = \frac{\phi_i L}{N} - \frac{L_{\mathrm{i}}}{\tau_{\mathrm{i}}},$$

where ϕ_i represents the net flux of neutrophils into tissue compartment i, weighted by the labeled fraction coming from the BM, whereas τ_i is the neutrophil mean lifetime in that same tissue compartment. The above ODEs can also be solved exactly in terms of quadratures by using the BM solution $L(t)$ together with the initial conditions $L_i(0) = 0$. Notice that once $L(t)$ starts to decrease (after day two) then, approximately, $L_i(t) \propto e^{-t/\tau_i}$.

To compute the fate mappings of CD11b$^+$ Ly6G$^+$ tdTomato$^+$ neutrophils in BM and tissues of iLy6Gtd$^{\mathrm{Tom}}$ mice displayed in Figure 1B, nonlinear regressions of decaying exponential functions $100e^{-(t-2)/\tau_{\mathrm{BM}}}$ and $100e^{-(t-3)/\tau_i}$ were performed using the MATLAB™ (R2019b) Statistics and Machine Learning toolbox command *fitnlm*. The datasets that were fitted corresponded to 2-7 days for BM and 3-7 days for blood and the other tissues, respectively. Mean lifetimes τ_{BM} and τ_i were estimated together with their respective confidence intervals (confidence levels at 95%) and p-values. From these, the half-lifetimes $t_{1/2}^{(\mathrm{BM})}$ in BM and $t_{1/2}^{(i)}$ in other tissues, as well as the confidence intervals, were found using the relations $t_{1/2}^{(\mathrm{BM})} = \log(2)\tau_{\mathrm{BM}}$ and $t_{1/2}^{(i)} = \log(2)\tau_i$. The values are displayed in Figure 1B and Fig.S1E.

Finally, to estimate the mean lifespans of tdTomato$^+$ labeled post-mitotic neutrophils in tissues we considered the 10% of those that were the most long-lived. Let $t_{10\%}^{(\mathrm{BM})}$ and $t_{10\%}^{(i)}$ denote the corresponding mean lifespans in BM and tissue i, respectively. Using the above decaying exponential functions $100e^{-(t-2)/\tau_{\mathrm{BM}}}$ and $100e^{-(t-3)/\tau_i}$, together with the obtained mean lifetimes, we computed the mean lifespans as $t_{10\%}^{(\mathrm{BM})} = \log(10)\tau_{\mathrm{BM}}$

and $t_{10\%}^{(i)} = \log(10)\tau_i$. Their values, together with their corresponding confidence intervals (confidence levels at 95%), are shown in Fig.S1E.

Quantification and statistical analysis

Data from experiments are represented as mean values ± SEM. All parameters analyzed followed normal distribution as tested by D'Agostino-Pearson test unless indicated in the figure legend. Unpaired two-tailed t-test was used when 2 groups were compared, and comparison of more than two data sets was done using one-way analysis of variance (ANOVA) with Turkey's post-test or two-way ANOVA. Log-rank analysis was used for Kaplan-Meier survival curves. Statistical analysis were performed using GraphPad software. Statistics on the RNA sequencing and ATAC sequencing are indicated in the analysis section. A p-value below 0.05 was considered statistically significant; non-significant differences (n.s.) are indicated accordingly, and P values ≤0.05 were considered statistically significant (*). P values P ≤ 0.01 (**) and P ≤ 0.001 (***), as well as nonsignificant differences (n.s.), are indicated accordingly.

Supplemental item titles

Supplemental Tables

Table S1 Differentially expressed genes in neutrophils from the single cell RNA sequencing analysis. Related to Figure 2.

Table S2 Differentially expressed genes in tissue neutrophils from the bulk RNA-sequencing analysis and LRT analysis of differentially accessible peaks in tissue neutrophils from the ATAC-sequencing analysis. Related to Figure 3.

Table S3 Differentially expressed genes in neutrophils from specific pathogen-free (SPF) and germ-free (GF) mice. Related to Figure 4.

Table S4 Differentially expressed gene lists and results from IPA analysis. Related to Figure 5.

Table S5 Angiogenic gene list used for the angiogenic score and gene list used for Nanostring profiling. Related to Figure 5 and 6.

Supplementary Movies

Video S1: Intravascular crawling of wild type and CXCR4$^{\Delta N}$ Ly6G^{+} neutrophils (grey) in the lung capillaries by intravital imaging. Related to Figure 6.

References

Adrover, J.M., Aroca-Crevilén, A., Crainiciuc, G., Ostos, F., Rojas-Vega, Y., Rubio-Ponce, A., Cilloniz, C., Bonzón-Kulichenko, E., Calvo, E., Rico, D.*, et al.* (2020). Programmed "disarming" of the neutrophil proteome reduces the magnitude of inflammation. Nat Immunol *In Press*.

Adrover, J.M., Del Fresno, C., Crainiciuc, G., Cuartero, M.I., Casanova-Acebes, M., Weiss, L.A., Huerga-Encabo, H., Silvestre-Roig, C., Rossaint, J., Cossio, I.*, et al.* (2019). A Neutrophil Timer Coordinates Immune Defense and Vascular Protection. Immunity *50*, 390-402 e310.

Bartels, M., Govers, A.M., Fleskens, V., Lourenco, A.R., Pals, C.E., Vervoort, S.J., van Gent, R., Brenkman, A.B., Bierings, M.B., Ackerman, S.J.*, et al.* (2015). Acetylation of C/EBPepsilon is a prerequisite for terminal neutrophil differentiation. Blood *125*, 1782-1792.

Becher, B., Schlitzer, A., Chen, J., Mair, F., Sumatoh, H.R., Teng, K.W., Low, D., Ruedl, C., Riccardi-Castagnoli, P., Poidinger, M.*, et al.* (2014). High-dimensional analysis of the murine myeloid cell system. Nat Immunol *15*, 1181-1189.

Bonnardel, J., T'Jonck, W., Gaublomme, D., Browaeys, R., Scott, C.L., Martens, L., Vanneste, B., De Prijck, S., Nedospasov, S.A., Kremer, A.*, et al.* (2019). Stellate Cells, Hepatocytes, and Endothelial Cells Imprint the Kupffer Cell Identity on Monocytes Colonizing the Liver Macrophage Niche. Immunity *51*, 638-654 e639.

Bowers, E., Slaughter, A., Frenette, P.S., Kuick, R., Pello, O.M., and Lucas, D. (2018). Granulocyte-derived TNFalpha promotes vascular and hematopoietic regeneration in the bone marrow. Nature medicine *24*, 95-102.

Bray, N.L., Pimentel, H., Melsted, P., and Pachter, L. (2016). Near-optimal probabilistic RNA-seq quantification. Nat Biotechnol *34*, 525-527.

Buch, T., Heppner, F.L., Tertilt, C., Heinen, T.J., Kremer, M., Wunderlich, F.T., Jung, S., and Waisman, A. (2005). A Cre-inducible diphtheria toxin receptor mediates cell lineage ablation after toxin administration. Nat Methods *2*, 419-426.

Buenrostro, J.D., Giresi, P.G., Zaba, L.C., Chang, H.Y., and Greenleaf, W.J. (2013). Transposition of native chromatin for fast and sensitive epigenomic profiling of open chromatin, DNA-binding proteins and nucleosome position. Nat Methods *10*, 1213-1218.

Butler, A., Hoffman, P., Smibert, P., Papalexi, E., and Satija, R. (2018). Integrating single-cell transcriptomic data across different conditions, technologies, and species. Nat Biotechnol *36*, 411-420.

Casanova-Acebes, M., Nicolas-Avila, J.A., Li, J.L., Garcia-Silva, S., Balachander, A., Rubio-Ponce, A., Weiss, L.A., Adrover, J.M., Burrows, K., N, A.G.*, et al.* (2018). Neutrophils instruct homeostatic and pathological states in naive tissues. J Exp Med *215*, 2778-2795.

Casanova-Acebes, M., Pitaval, C., Weiss, L.A., Nombela-Arrieta, C., Chevre, R., N, A.G., Kunisaki, Y., Zhang, D., van Rooijen, N., Silberstein, L.E.*, et al.* (2013). Rhythmic modulation of the hematopoietic niche through neutrophil clearance. Cell *153*, 1025-1035.

Christoffersson, G., Vagesjo, E., Vandooren, J., Liden, M., Massena, S., Reinert, R.B., Brissova, M., Powers, A.C., Opdenakker, G., and Phillipson, M. (2012). VEGF-A recruits a proangiogenic MMP-9-delivering neutrophil subset that induces angiogenesis in transplanted hypoxic tissue. Blood *120*, 4653-4662.

Coffelt, S.B., Wellenstein, M.D., and de Visser, K.E. (2016). Neutrophils in cancer: neutral no more. Nat Rev Cancer *16*, 431-446.

Cohen, M., Giladi, A., Gorki, A.D., Solodkin, D.G., Zada, M., Hladik, A., Miklosi, A., Salame, T.M., Halpern, K.B., David, E.*, et al.* (2018). Lung Single-Cell Signaling Interaction Map Reveals Basophil Role in Macrophage Imprinting. Cell *175*, 1031-1044 e1018.

Cuartero, M.I., Ballesteros, I., Moraga, A., Nombela, F., Vivancos, J., Hamilton, J.A., Corbi, A.L., Lizasoain, I., and Moro, M.A. (2013). N2 neutrophils, novel players in brain inflammation after stroke: modulation by the PPARgamma agonist rosiglitazone. Stroke *44*, 3498-3508.

Devi, S., Wang, Y., Chew, W.K., Lima, R., N, A.G., Mattar, C.N., Chong, S.Z., Schlitzer, A., Bakocevic, N., Chew, S.*, et al.* (2013). Neutrophil mobilization via plerixafor-mediated CXCR4 inhibition arises from lung demargination and blockade of neutrophil homing to the bone marrow. J Exp Med *210*, 2321-2336.

Engblom, C., Pfirschke, C., Zilionis, R., Da Silva Martins, J., Bos, S.A., Courties, G., Rickelt, S., Severe, N., Baryawno, N., Faget, J.*, et al.* (2017). Osteoblasts remotely supply lung tumors with cancer-promoting SiglecF(high) neutrophils. Science *358*.

Evrard, M., Kwok, I.W.H., Chong, S.Z., Teng, K.W.W., Becht, E., Chen, J., Sieow, J.L., Penny, H.L., Ching, G.C., Devi, S.*, et al.* (2018). Developmental Analysis of Bone Marrow Neutrophils Reveals Populations Specialized in Expansion, Trafficking, and Effector Functions. Immunity *48*, 364-379 e368.

Gentek, R., Ghigo, C., Hoeffel, G., Bulle, M.J., Msallam, R., Gautier, G., Launay, P., Chen, J., Ginhoux, F., and Bajenoff, M. (2018). Hemogenic Endothelial Fate Mapping Reveals Dual Developmental Origin of Mast Cells. Immunity *48*, 1160-1171 e1165.

Ginhoux, F., and Guilliams, M. (2016). Tissue-Resident Macrophage Ontogeny and Homeostasis. Immunity *44*, 439-449.

Gomez Perdiguero, E., Klapproth, K., Schulz, C., Busch, K., Azzoni, E., Crozet, L., Garner, H., Trouillet, C., de Bruijn, M.F., Geissmann, F.*, et al.* (2015). Tissue-resident macrophages originate from yolk-sac-derived erythro-myeloid progenitors. Nature *518*, 547-551.

Gosselin, D., Link, V.M., Romanoski, C.E., Fonseca, G.J., Eichenfield, D.Z., Spann, N.J., Stender, J.D., Chun, H.B., Garner, H., Geissmann, F.*, et al.* (2014). Environment drives selection and function of enhancers controlling tissue-specific macrophage identities. Cell *159*, 1327-1340.

Grassi, L., Pourfarzad, F., Ullrich, S., Merkel, A., Were, F., Carrillo-de-Santa-Pau, E., Yi, G., Hiemstra, I.H., Tool, A.T.J., Mul, E.*, et al.* (2018). Dynamics of Transcription Regulation in Human Bone Marrow Myeloid Differentiation to Mature Blood Neutrophils. Cell Rep *24*, 2784-2794.

Gupta, S., and Kaplan, M.J. (2016). The role of neutrophils and NETosis in autoimmune and renal diseases. Nature reviews Nephrology *12*, 402-413.

Hanna, R.N., Carlin, L.M., Hubbeling, H.G., Nackiewicz, D., Green, A.M., Punt, J.A., Geissmann, F., and Hedrick, C.C. (2011). The transcription factor NR4A1 (Nur77) controls bone marrow differentiation and the survival of Ly6C- monocytes. Nat Immunol *12*, 778-785.

Hasenberg, A., Hasenberg, M., Mann, L., Neumann, F., Borkenstein, L., Stecher, M., Kraus, A., Engel, D.R., Klingberg, A., Seddigh, P.*, et al.* (2015). Catchup: a mouse model for imaging-based tracking and modulation of neutrophil granulocytes. Nat Methods *12*, 445-452.

Hidalgo, A., Chilvers, E.R., Summers, C., and Koenderman, L. (2019). The Neutrophil Life Cycle. Trends Immunol *40*, 584-597.

Hoeffel, G., Chen, J., Lavin, Y., Low, D., Almeida, F.F., See, P., Beaudin, A.E., Lum, J., Low, I., Forsberg, E.C.*, et al.* (2015). C-Myb(+) erythro-myeloid progenitor-derived fetal monocytes give rise to adult tissue-resident macrophages. Immunity *42*, 665-678.

Hoogendijk, A.J., Pourfarzad, F., Aarts, C.E.M., Tool, A.T.J., Hiemstra, I.H., Grassi, L., Frontini, M., Meijer, A.B., van den Biggelaar, M., and Kuijpers, T.W. (2019). Dynamic Transcriptome-Proteome Correlation Networks Reveal Human Myeloid Differentiation and Neutrophil-Specific Programming. Cell Rep *29*, 2505-2519 e2504.

Janich, P., Pascual, G., Merlos-Suarez, A., Batlle, E., Ripperger, J., Albrecht, U., Cheng, H.Y., Obrietan, K., Di Croce, L., and Benitah, S.A. (2011). The circadian molecular clock creates epidermal stem cell heterogeneity. Nature *480*, 209-214.

Keren-Shaul, H., Spinrad, A., Weiner, A., Matcovitch-Natan, O., Dvir-Szternfeld, R., Ulland, T.K., David, E., Baruch, K., Lara-Astaiso, D., Toth, B.*, et al.* (2017). A Unique Microglia Type Associated with Restricting Development of Alzheimer's Disease. Cell *169*, 1276-1290 e1217.

Kim, M.H., Yang, D., Kim, M., Kim, S.Y., Kim, D., and Kang, S.J. (2017). A late-lineage murine neutrophil precursor population exhibits dynamic changes during demand-adapted granulopoiesis. Scientific reports *7*, 39804.

Kwok, I., Becht, E., Xia, Y., Ng, M., Teh, Y.C., Tan, L., Evrard, M., Li, J.L.Y., Tran, H.T.N., Tan, Y.*, et al.* (2020). Combinatorial Single-Cell Analyses of Granulocyte-Monocyte Progenitor Heterogeneity Reveals an Early Uni-potent Neutrophil Progenitor. Immunity.

Lavin, Y., Kobayashi, S., Leader, A., Amir, E.D., Elefant, N., Bigenwald, C., Remark, R., Sweeney, R., Becker, C.D., Levine, J.H.*, et al.* (2017). Innate Immune Landscape in Early Lung Adenocarcinoma by Paired Single-Cell Analyses. Cell *169*, 750-765 e717.

Lavin, Y., Mortha, A., Rahman, A., and Merad, M. (2015). Regulation of macrophage development and function in peripheral tissues. Nat Rev Immunol *15*, 731-744.

Lavin, Y., Winter, D., Blecher-Gonen, R., David, E., Keren-Shaul, H., Merad, M., Jung, S., and Amit, I. (2014). Tissue-resident macrophage enhancer landscapes are shaped by the local microenvironment. Cell *159*, 1312-1326.

Li, B., and Dewey, C.N. (2011). RSEM: accurate transcript quantification from RNA-Seq data with or without a reference genome. BMC Bioinformatics *12*, 323.

Li, Z., Liu, S., Xu, J., Zhang, X., Han, D., Liu, J., Xia, M., Yi, L., Shen, Q., Xu, S.*, et al.* (2018). Adult Connective Tissue-Resident Mast Cells Originate from Late Erythro-Myeloid Progenitors. Immunity *49*, 640-653 e645.

Liu, Z., Gu, Y., Chakarov, S., Bleriot, C., Kwok, I., Chen, X., Shin, A., Huang, W., Dress, R.J., Dutertre, C.A.*, et al.* (2019). Fate Mapping via Ms4a3-Expression History Traces Monocyte-Derived Cells. Cell *178*, 1509-1525 e1519.

Ma, Y., Yabluchanskiy, A., Iyer, R.P., Cannon, P.L., Flynn, E.R., Jung, M., Henry, J., Cates, C.A., Deleon-Pennell, K.Y., and Lindsey, M.L. (2016). Temporal neutrophil polarization following myocardial infarction. Cardiovasc Res *110*, 51-61.

Madisen, L., Zwingman, T.A., Sunkin, S.M., Oh, S.W., Zariwala, H.A., Gu, H., Ng, L.L., Palmiter, R.D., Hawrylycz, M.J., Jones, A.R.*, et al.* (2010). A robust and high-throughput Cre reporting and characterization system for the whole mouse brain. Nat Neurosci *13*, 133-140.

Mass, E., Jacome-Galarza, C.E., Blank, T., Lazarov, T., Durham, B.H., Ozkaya, N., Pastore, A., Schwabenland, M., Chung, Y.R., Rosenblum, M.K.*, et al.* (2017). A somatic mutation in erythro-myeloid progenitors causes neurodegenerative disease. Nature *549*, 389-393.

Massena, S., Christoffersson, G., Vagesjo, E., Seignez, C., Gustafsson, K., Binet, F., Herrera Hidalgo, C., Giraud, A., Lomei, J., Westrom, S.*, et al.* (2015). Identification and characterization of VEGF-A-responsive neutrophils expressing CD49d, VEGFR1, and CXCR4 in mice and humans. Blood *126*, 2016-2026.

McGrath, K.E., Frame, J.M., Fegan, K.H., Bowen, J.R., Conway, S.J., Catherman, S.C., Kingsley, P.D., Koniski, A.D., and Palis, J. (2015). Distinct Sources of Hematopoietic Progenitors Emerge before HSCs and Provide Functional Blood Cells in the Mammalian Embryo. Cell Rep *11*, 1892-1904.

Mildner, A., Schonheit, J., Giladi, A., David, E., Lara-Astiaso, D., Lorenzo-Vivas, E., Paul, F., Chappell-Maor, L., Priller, J., Leutz, A.*, et al.* (2017). Genomic Characterization of Murine Monocytes Reveals C/EBPbeta Transcription Factor Dependence of Ly6C(-) Cells. Immunity *46*, 849-862 e847.

Natoli, G., and Ostuni, R. (2019). Adaptation and memory in immune responses. Nat Immunol *20*, 783-792.

Ng, L.G., Ostuni, R., and Hidalgo, A. (2019). Heterogeneity of neutrophils. Nat Rev Immunol *19*, 255-265.

Nicolas-Avila, J.A., Adrover, J.M., and Hidalgo, A. (2017). Neutrophils in Homeostasis, Immunity, and Cancer. Immunity *46*, 15-28.

Nie, Y., Waite, J., Brewer, F., Sunshine, M.J., Littman, D.R., and Zou, Y.R. (2004). The role of CXCR4 in maintaining peripheral B cell compartments and humoral immunity. J Exp Med *200*, 1145-1156.

Passegue, E., Wagner, E.F., and Weissman, I.L. (2004). JunB deficiency leads to a myeloproliferative disorder arising from hematopoietic stem cells. Cell *119*, 431-443.

Pillay, J., den Braber, I., Vrisekoop, N., Kwast, L.M., de Boer, R.J., Borghans, J.A., Tesselaar, K., and Koenderman, L. (2010). In vivo labeling with 2H2O reveals a human neutrophil lifespan of 5.4 days. Blood *116*, 625-627.

Pimentel, H., Bray, N.L., Puente, S., Melsted, P., and Pachter, L. (2017). Differential analysis of RNA-seq incorporating quantification uncertainty. Nat Methods *14*, 687-690.

Puga, I., Cols, M., Barra, C.M., He, B., Cassis, L., Gentile, M., Comerma, L., Chorny, A., Shan, M., Xu, W.*, et al.* (2011). B cell-helper neutrophils stimulate the diversification and production of immunoglobulin in the marginal zone of the spleen. Nat Immunol *13*, 170-180.

Ritchie, M.E., Phipson, B., Wu, D., Hu, Y., Law, C.W., Shi, W., and Smyth, G.K. (2015). limma powers differential expression analyses for RNA-sequencing and microarray studies. Nucleic Acids Res *43*, e47.

Robinson, M.D., McCarthy, D.J., and Smyth, G.K. (2010). edgeR: a Bioconductor package for differential expression analysis of digital gene expression data. Bioinformatics *26*, 139-140.

Sagiv, J.Y., Michaeli, J., Assi, S., Mishalian, I., Kisos, H., Levy, L., Damti, P., Lumbroso, D., Polyansky, L., Sionov, R.V.*, et al.* (2015). Phenotypic diversity and plasticity in circulating neutrophil subpopulations in cancer. Cell Rep *10*, 562-573.

Schageman, J., Zeringer, E., Li, M., Barta, T., Lea, K., Gu, J., Magdaleno, S., Setterquist, R., and Vlassov, A.V. (2013). The complete exosome workflow solution: from isolation to characterization of RNA cargo. Biomed Res Int *2013*, 253957.

Silvestre-Roig, C., Hidalgo, A., and Soehnlein, O. (2016). Neutrophil heterogeneity: implications for homeostasis and pathogenesis. Blood *127*, 2173-2181.

Singhal, S., Bhojnagarwala, P.S., O'Brien, S., Moon, E.K., Garfall, A.L., Rao, A.S., Quatromoni, J.G., Stephen, T.L., Litzky, L., Deshpande, C.*, et al.* (2016). Origin and Role of a Subset of Tumor-Associated Neutrophils with Antigen-Presenting Cell Features in Early-Stage Human Lung Cancer. Cancer Cell *30*, 120-135.

Stuart, T., Butler, A., Hoffman, P., Hafemeister, C., Papalexi, E., Mauck, W.M., 3rd, Hao, Y., Stoeckius, M., Smibert, P., and Satija, R. (2019). Comprehensive Integration of Single-Cell Data. Cell *177*, 1888-1902 e1821.

Sugiyama, T., Kohara, H., Noda, M., and Nagasawa, T. (2006). Maintenance of the hematopoietic stem cell pool by CXCL12-CXCR4 chemokine signaling in bone marrow stromal cell niches. Immunity *25*, 977-988.

Summers, C., Rankin, S.M., Condliffe, A.M., Singh, N., Peters, A.M., and Chilvers, E.R. (2010). Neutrophil kinetics in health and disease. Trends Immunol *31*, 318-324.

Susaki, E.A., Tainaka, K., Perrin, D., Kishino, F., Tawara, T., Watanabe, T.M., Yokoyama, C., Onoe, H., Eguchi, M., Yamaguchi, S.*, et al.* (2014). Whole-brain imaging with single-cell resolution using chemical cocktails and computational analysis. Cell *157*, 726-739.

Tsuda, Y., Takahashi, H., Kobayashi, M., Hanafusa, T., Herndon, D.N., and Suzuki, F. (2004). Three different neutrophil subsets exhibited in mice with different susceptibilities to infection by methicillin-resistant Staphylococcus aureus. Immunity *21*, 215-226.

Wang, J., Hossain, M., Thanabalasuriar, A., Gunzer, M., Meininger, C., and Kubes, P. (2017). Visualizing the function and fate of neutrophils in sterile injury and repair. Science *358*, 111-116.

Wynn, T.A., Chawla, A., and Pollard, J.W. (2013). Macrophage biology in development, homeostasis and disease. Nature *496*, 445-455.

Yipp, B.G., Kim, J.H., Lima, R., Zbytnuik, L.D., Petri, B., Swanlund, N., Ho, M., Szeto, V.G., Tak, T., Koenderman, L.*, et al.* (2017). The Lung is a Host Defense Niche for Immediate Neutrophil-Mediated Vascular Protection. Sci Immunol *2*.

Zhu, Y.P., Padgett, L., Dinh, H.Q., Marcovecchio, P., Blatchley, A., Wu, R., Ehinger, E., Kim, C., Mikulski, Z., Seumois, G.*, et al.* (2018). Identification of an Early Unipotent Neutrophil Progenitor with Pro-tumoral Activity in Mouse and Human Bone Marrow. Cell Rep *24*, 2329-2341 e2328.

Zilionis, R., Engblom, C., Pfirschke, C., Savova, V., Zemmour, D., Saatcioglu, H.D., Krishnan, I., Maroni, G., Meyerovitz, C.V., Kerwin, C.M.*, et al.* (2019). Single-Cell Transcriptomics of Human and Mouse Lung Cancers Reveals Conserved Myeloid Populations across Individuals and Species. Immunity *50*, 1317-1334 e1310.

KEY RESOURCES TABLE

REAGENT or	SOURCE	IDENTIFIER
Antibodies		
Anti-Mouse CD3e Percp/Cy5.5 (Clone 17A2)	BioLegend	RRID:AB_1595597
Anti-F4/80-PE.Cy7 (clone BM8)	eBioscience	RRID:AB_469653
Ly6G-Dylight 650 (Clone 1A8)	BioXcell (conjugated in-house)	RRID:AB_1107721
Ly6G-FITC (Clone 1A8)	eBioscience	RRID:AB_2572532
CD45-PerCP-Cy5.5 (Clone 30-F11)	Biolegend	RRID:AB_893344
CD11b-PE (Clone M1/70)	Tonbo Biosciences	RRID:AB_2621746
CD11b-FITC (Clone M1/70)	BD	RRID:AB_394774
Anti-CD11b-Bv510 (Clone M1/70)	Biolegend	RRID:AB_2561390
CXCR2-PerCP-Cy5.5 (Clone SA044G4)	Biolegend	RRID:AB_2565695
CXCR4-APC (Clone 2B11)	eBioscience	RRID:AB_10670877
Anti-IL1B-APC (Clone NJTEN3)	eBioscience	RRID:AB_10670739
Ly6C-FITC (Clone HK1.4)	Biolegend	RRID:AB_1186134
Anti-Mouse/Rat Ki-67 eFluor 660 (Clone SolA15)	eBioscienece	RRID:AB_2574235
Anti-Mouse CD49b (pan-NK cells) PE (clone HMα2)	BD	RRID:AB_397108
Anti-CD45-PerCP.Cy5.5 (clone 30-F11)	Biolegend	RRID:AB_893340
Anti-Mouse CD45R-BV220 APC-Cy7 (clone B220)	BD	RRID:AB_394335
Anti-CD45.1-PerCP.Cy5.5 (Clone A20)	TonboBioscience	RRID:AB_2621893
anti-mouse CD144 (VE-cadherin) APC	Biolegend	RRID:AB_10679039
Anti-Mouse NK1.1 AF488 (Clone Pk136)	Biolegend	RRID:AB_313392

Chicken Anti-GFP (polyclonal)	Thermo Fisher	RRID:AB_2534023
Anti-Mouse S100-A9 (Clone 2B10)	Abcam	RRID:AB_10862594
Rabbit monoclonal anti-ERG (Clone EPR3864)	Abcam	RRID:AB_2630401
Anti-Mouse CD74 AF647 (Clone: in1/CD74)	BioLegend	RRID:AB_2632608
Anti-Mouse CR1/2 (Clone:7E/9)	Biolegend	RRID:AB_940403
Anti-Mouse CD49d-APC (Clone R1-2)	Biolegend	RRID:AB_2565776
Anti-Mouse CD115 (c-fms) PE	eBioscience	RRID:AB_465809
Anti-Mouse CD117 (c-Kit) PE-Cy7 (Clone 2B8)	eBioscience	RRID:AB_469644
Anti-CD31 PE-Cy7 (Clone: 390)	eBioscience	RRID:AB_2716949
F4/80 antibody (Clone :A3-1)	Abcam	RRID:AB_1140040
CD45R/B220 antibody	BD	RRID: AB_396673
CD31 antibody	Abcam	RRID: AB_726362
Experimental Models: Organisms/Strains		
WT	Charles River	C57BL/6
$Mrp8^{CRE}$	Passegué et al. 2004	B6.Cg-Tg(S100A8-cre,-EGFP)1Ilw
$Cxcr4^{fl/fl}$	Nie et al. 2004	$B6.129P2\text{-}Cxcr4^{tm2Yzo}$
$Mrp8^{CRE}$; $Cxcr4^{fl/fl}$ ($Cxcr4^{\Delta N}$)	This paper	N/A
$Nr4a1^{f/f}$	Skarnes et al. 2011	Nr4a1tm1a(EUCOMM)Wtsi
$Mrp8^{CRE}$; $Nr4a1^{f/f}$ ($Nr4a1^{\Delta N}$)	This paper	N/A
$Arntl^{fl/fl}$	Janich et al. 2011	$B6.129S4(Cg)\text{-}Arntl^{tm1Weit}$
$Mrp8^{CRE}$; $Arntl^{fl/fl}$ ($Arntl^{\Delta N}$)	This paper	N/A
$Cxcl12^{GFP}$	Ara et al. 2003	Cxcl12tm2Tng
$Lyz2^{GFP}$	Faust et al. 2000	$B6.129P\text{-}Lyz2^{tm1(EGFP)1.1Graf/Mmmh}$
$Rosa26^{tdTomato}$	Madisen et al. 2010	B6.Cg-Gt(ROSA)26Sortm14(CAG-tdTomato)Hze/J
$Rosa26^{DTR}$	Buch et al. 2005	C57BL/6-Gt(ROSA)26Sortm1(HBEGF)Awai/J
$Ly6g^{CRE}$	Hasenberg et al., 2015	N/A
$Ly6g^{CREERT2}$	This paper	N/A

Chemicals, Peptides, and Recombinant Proteins		
Diphteria Toxin	Calbiochem	CAT# 322326
Tamoxifen	Sigma	CAT# T5648
Oligonucleotides		
Primers for qPCR, see method details	This paper	N/A
Critical commercial Assays		
nCounter XT Elements XT-ELE-048-P1TS	Nanostring®	041121000004
Counter Master Kit NAA-AKIT-012	Nanostring®	041100052-K
Software and Algorithms		
ImageJ	NIH	Schindelin J. et al 2015
Imaris	Bitplane	RRID:SCR_007370
Genesis	TÜ Graz	RRID:SCR_015775
Prism	Graphpad	RRID:SCR_002798
Flowjo vX	Treestar	RRID:SCR_008520
Cutadapt	NBIS	https://cutadapt.readthedocs.io/en/stable/
RSEM	PMID 21816040	http://deweylab.github.io/RSEM/
R	The R Foundation	https://www.r-project.org/
Limma	PMID 25605792	https://bioconductor.org/packages/release/bioc/html/limma.html
Seurat	PMID 29608179	https://satijalab.org/seurat/
kallisto	PMID 27043002	https://pachterlab.github.io/kallisto/
sleuth	PMID 28581496	https://pachterlab.github.io/sleuth/

Figure 1

Click here to access/download;Figure;Figure_1 half lives_New-01.tif

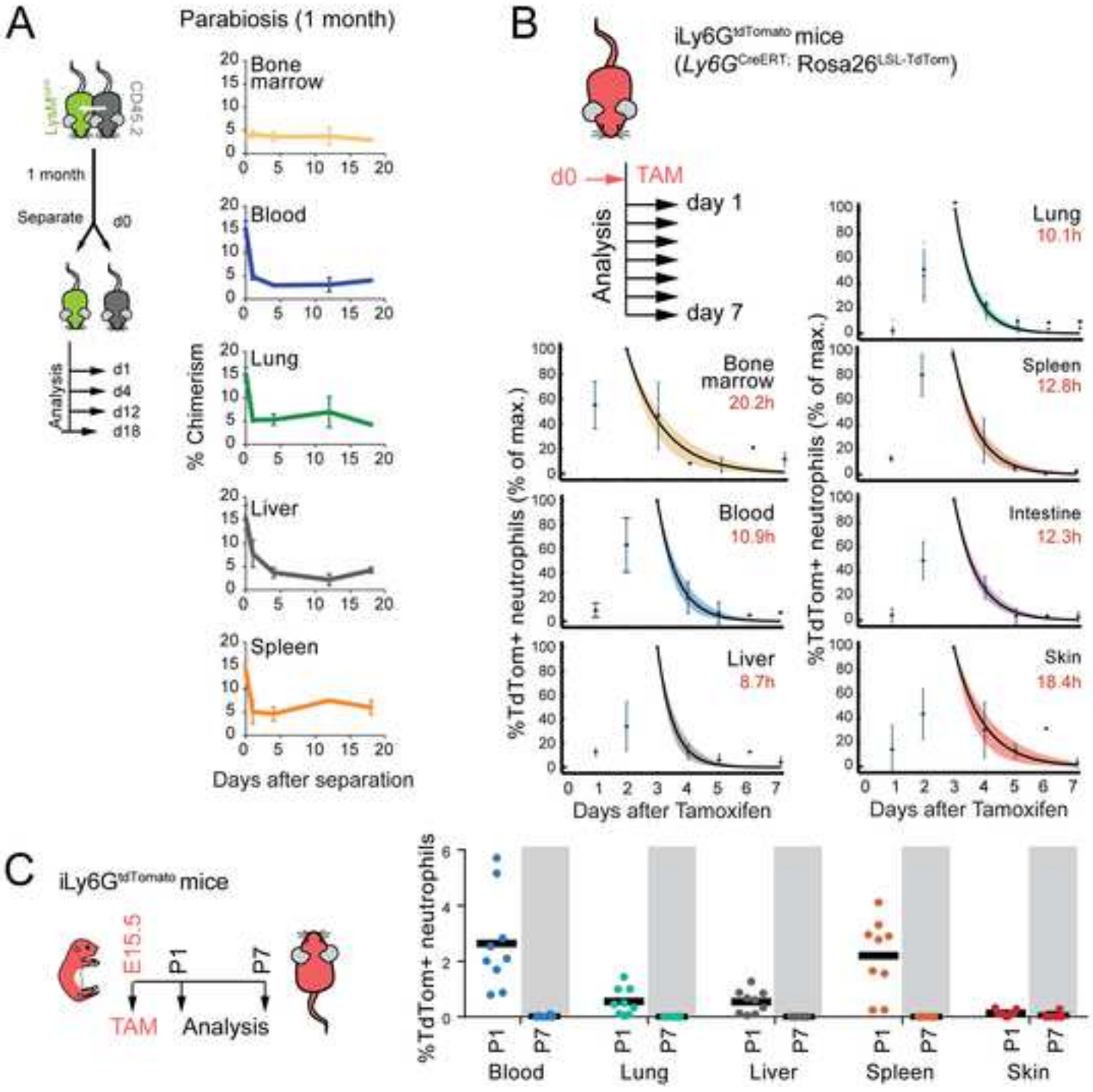

Figure 2

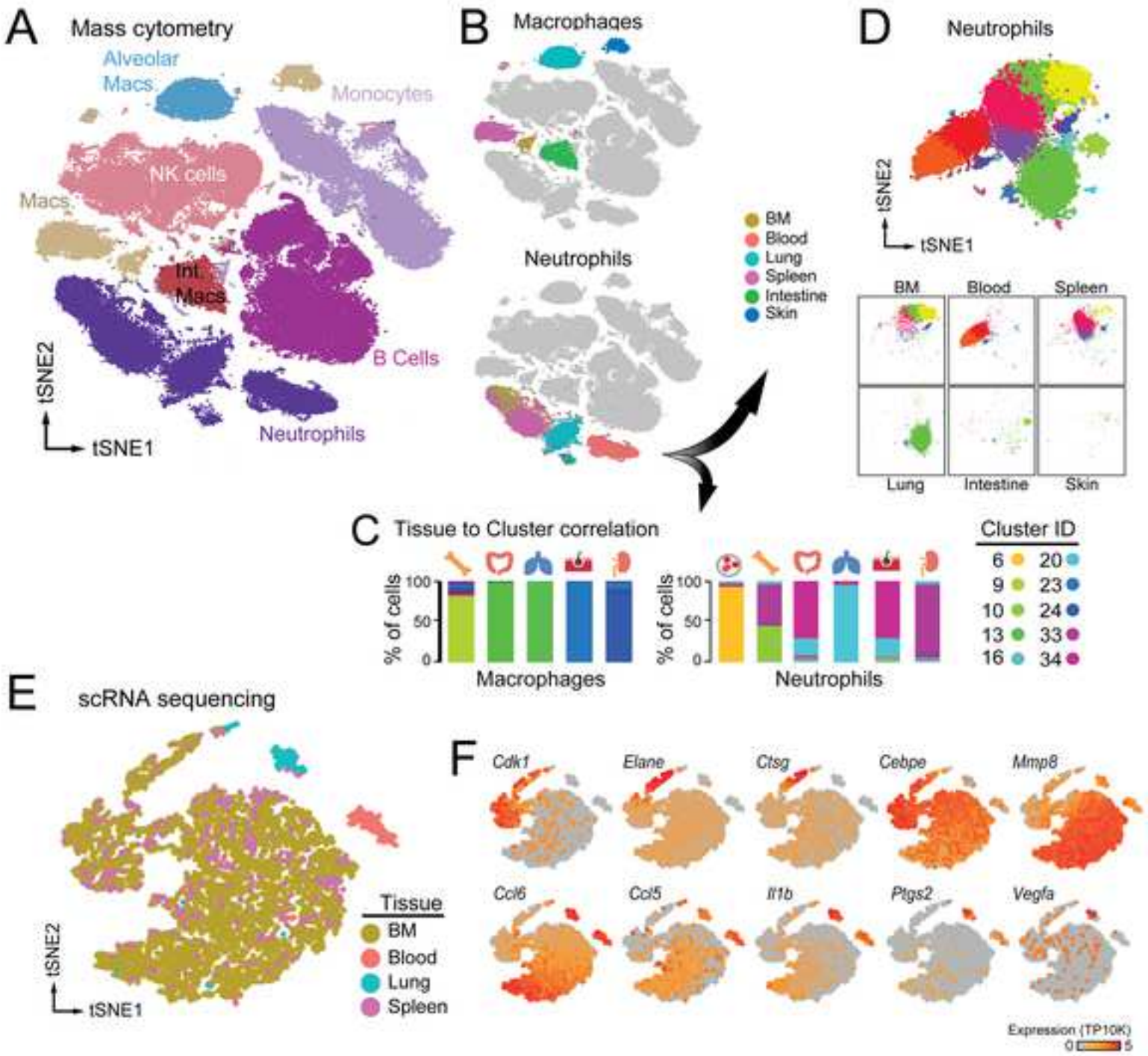

Figure 3

Click here to access/download;Figure;Figure_3 ATACseq+Bulk-01.tif

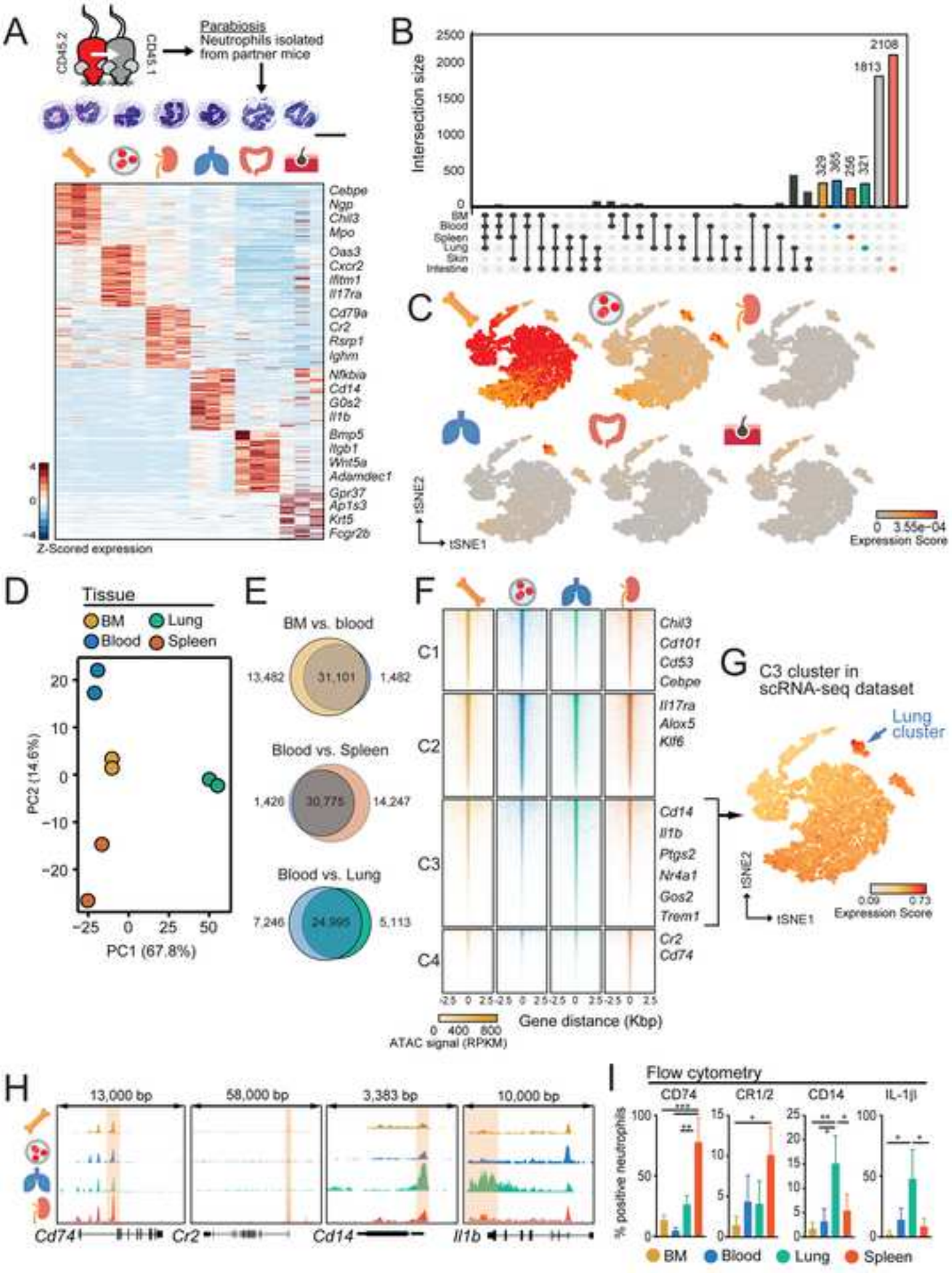

Figure 4

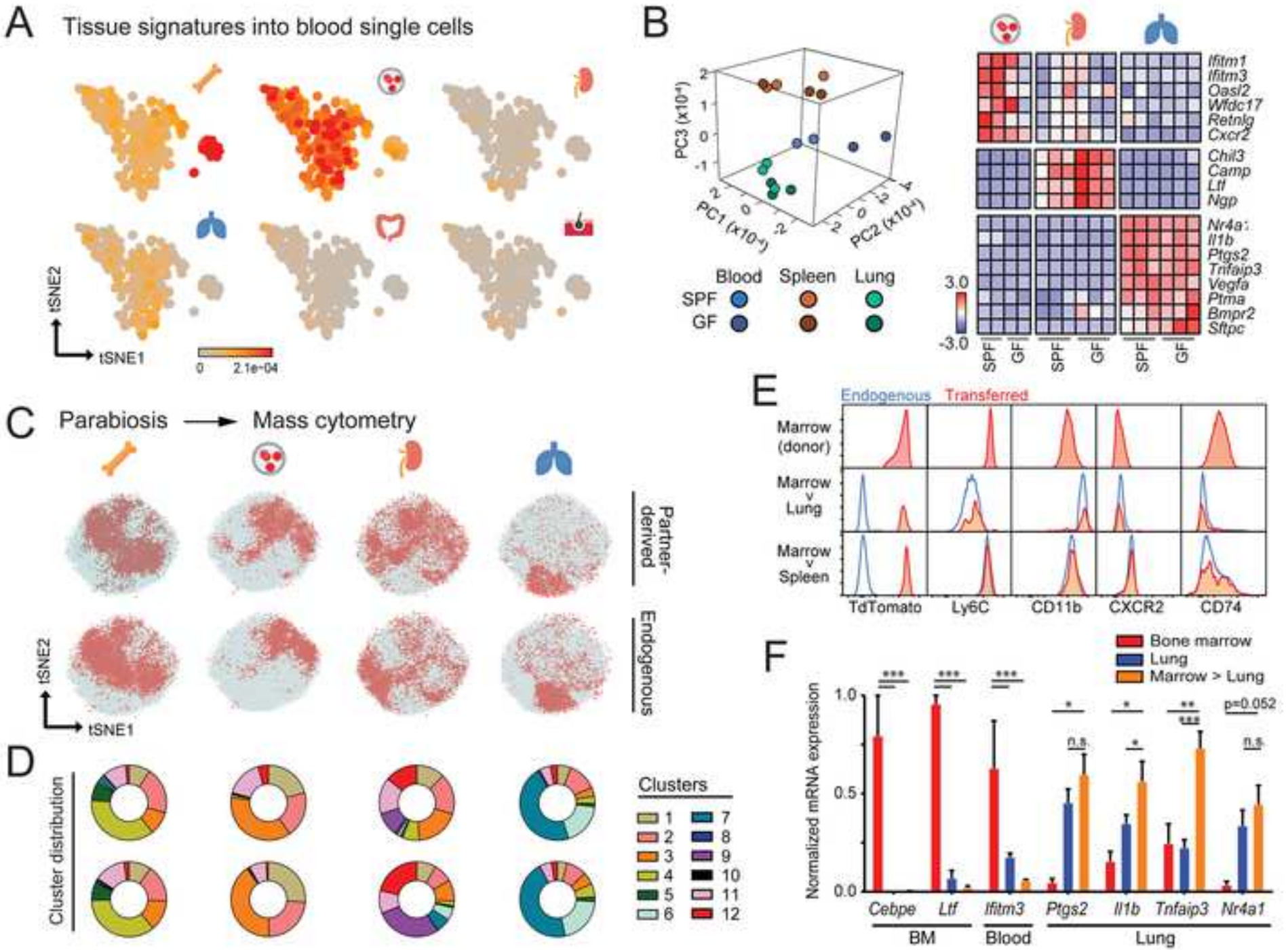

Figure 5

Click here to access/download;Figure;Figure_5_leuko + angio-01.tif

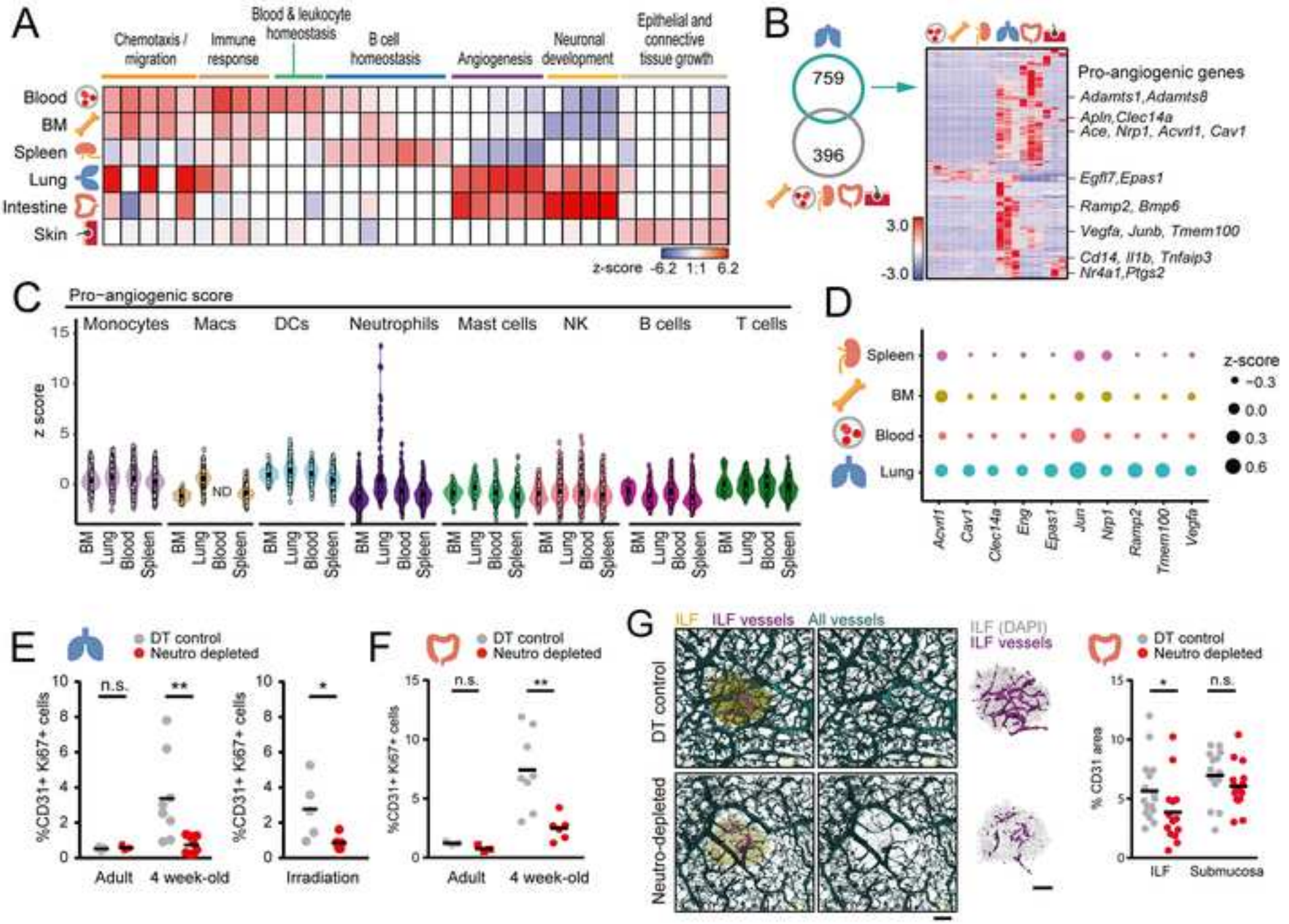

Figure 6

Click here to access/download;Figure;Figure_6_CXCR4-01.tif

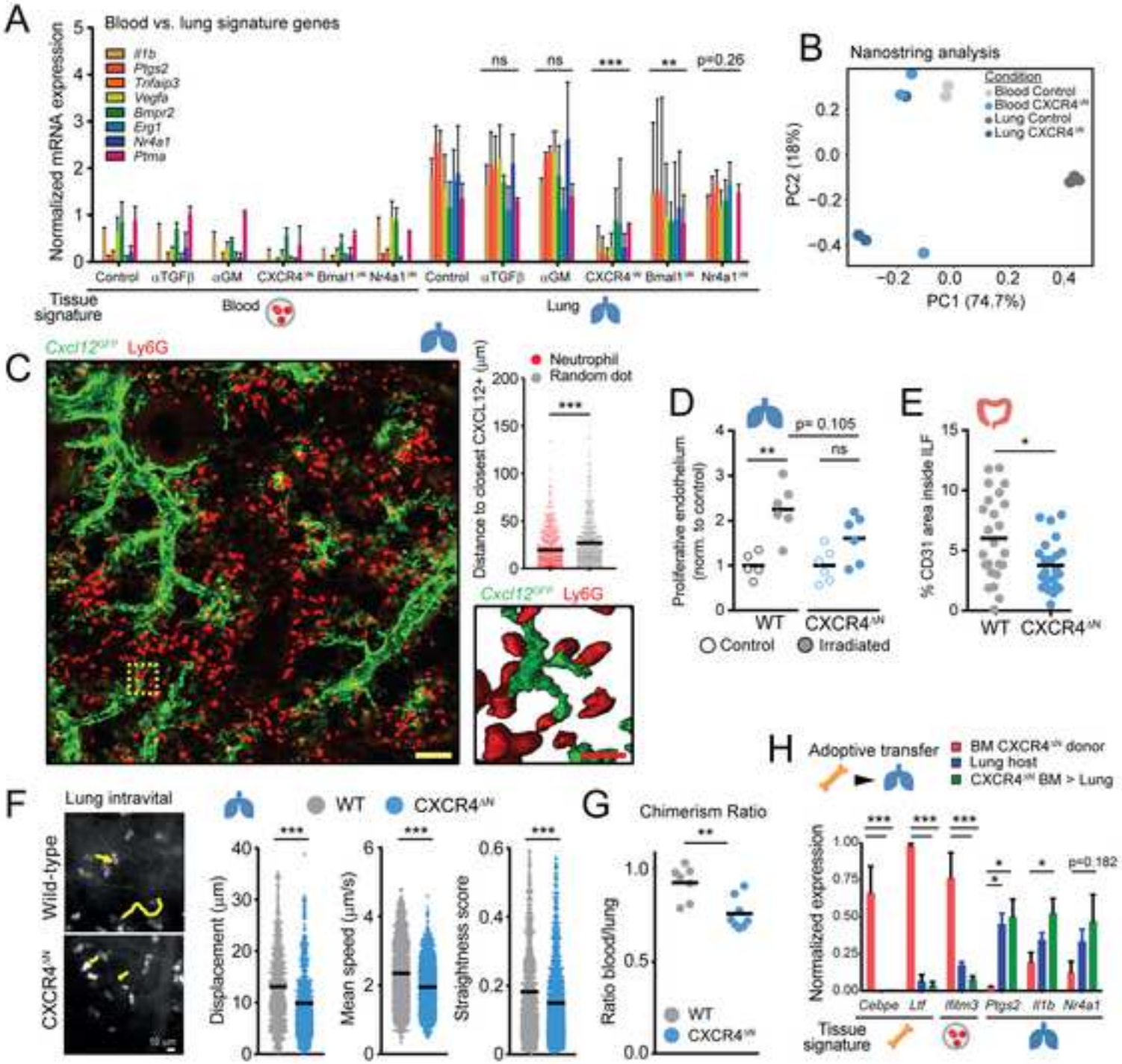

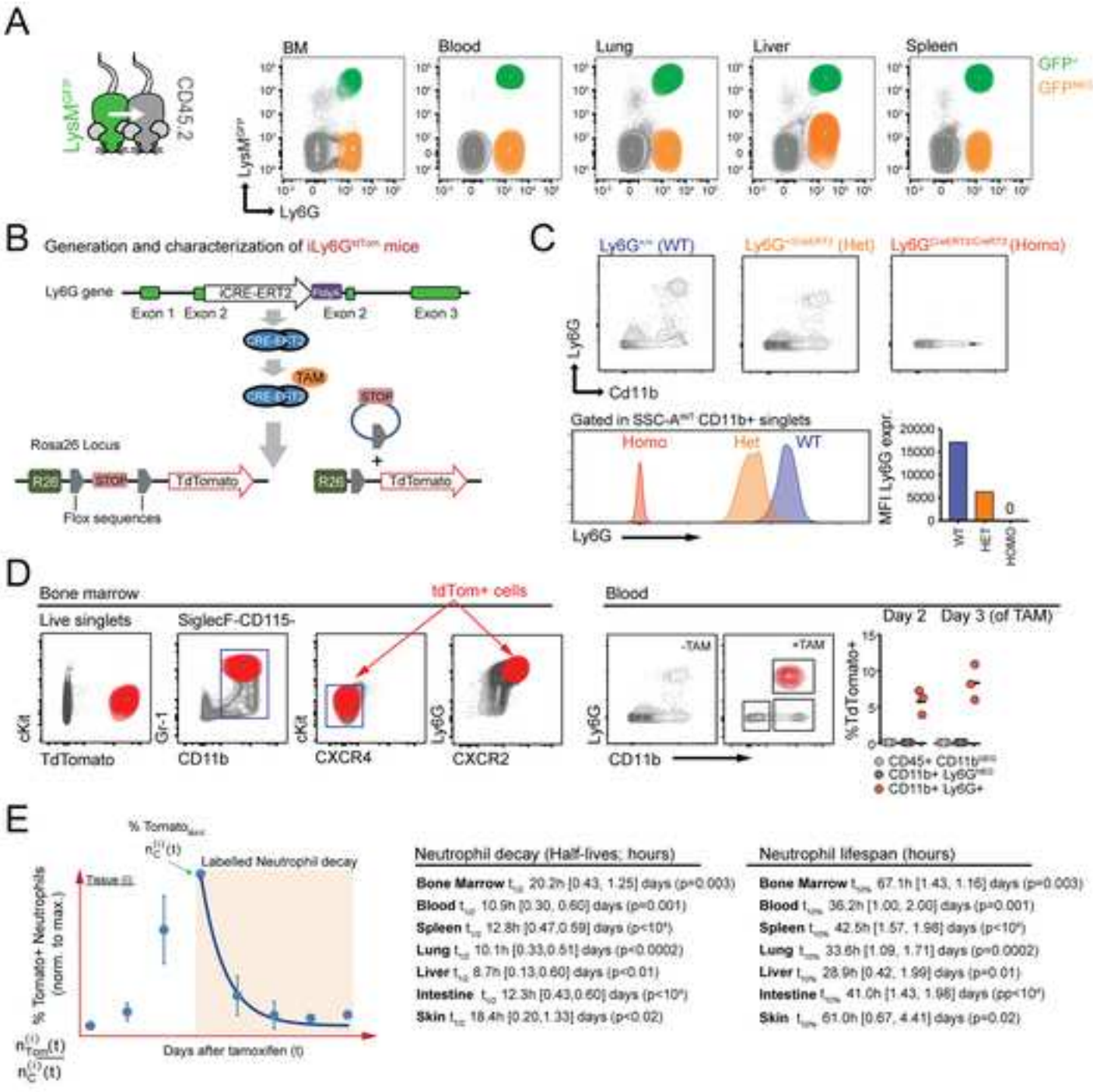

FigS2

Click here to access/download;Supplemental Figure;FigS2_merged-01.tif

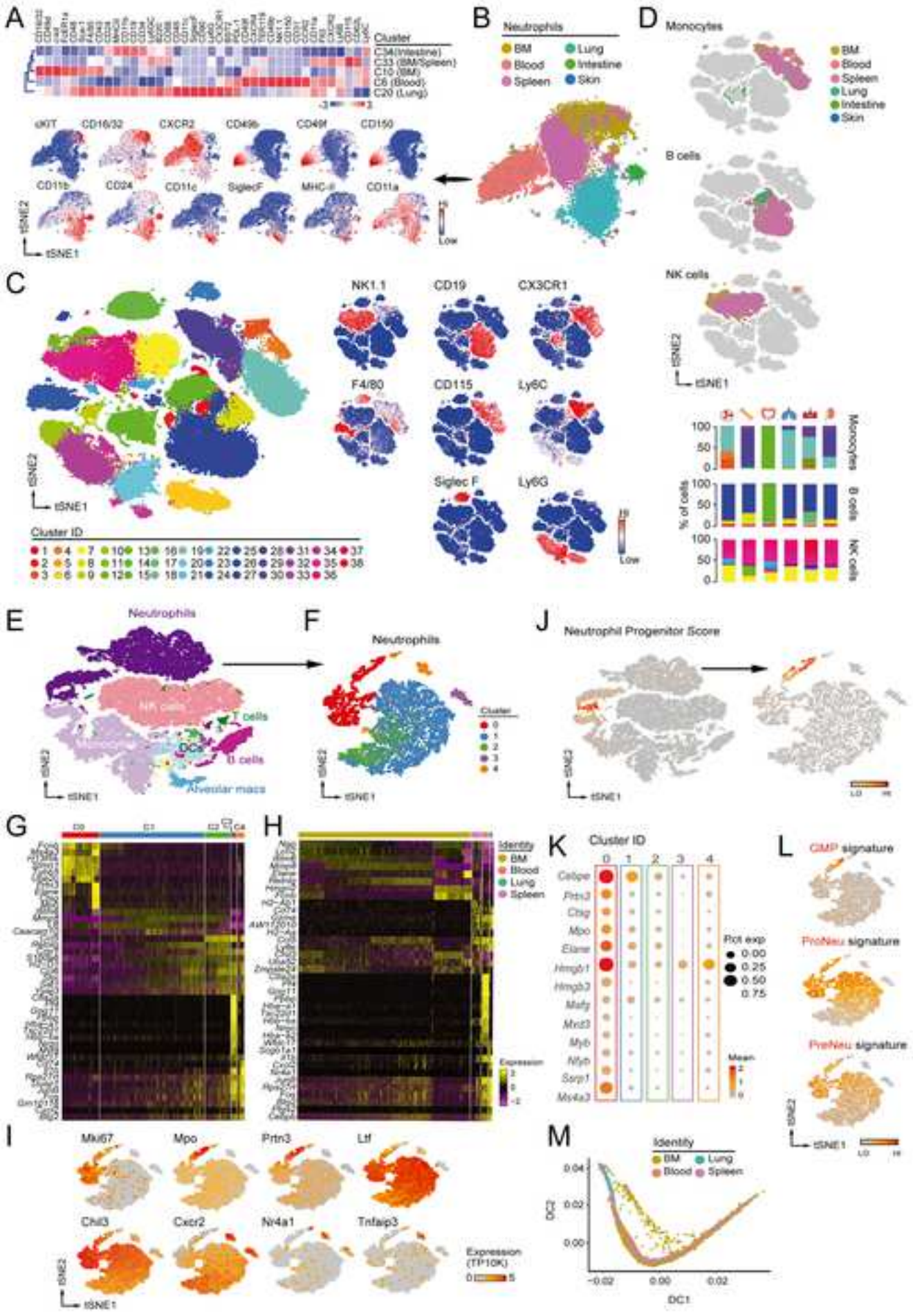

FigS3

Click here to access/download;Supplemental Figure;FigS3_ATAC + bulk_New-01.tif

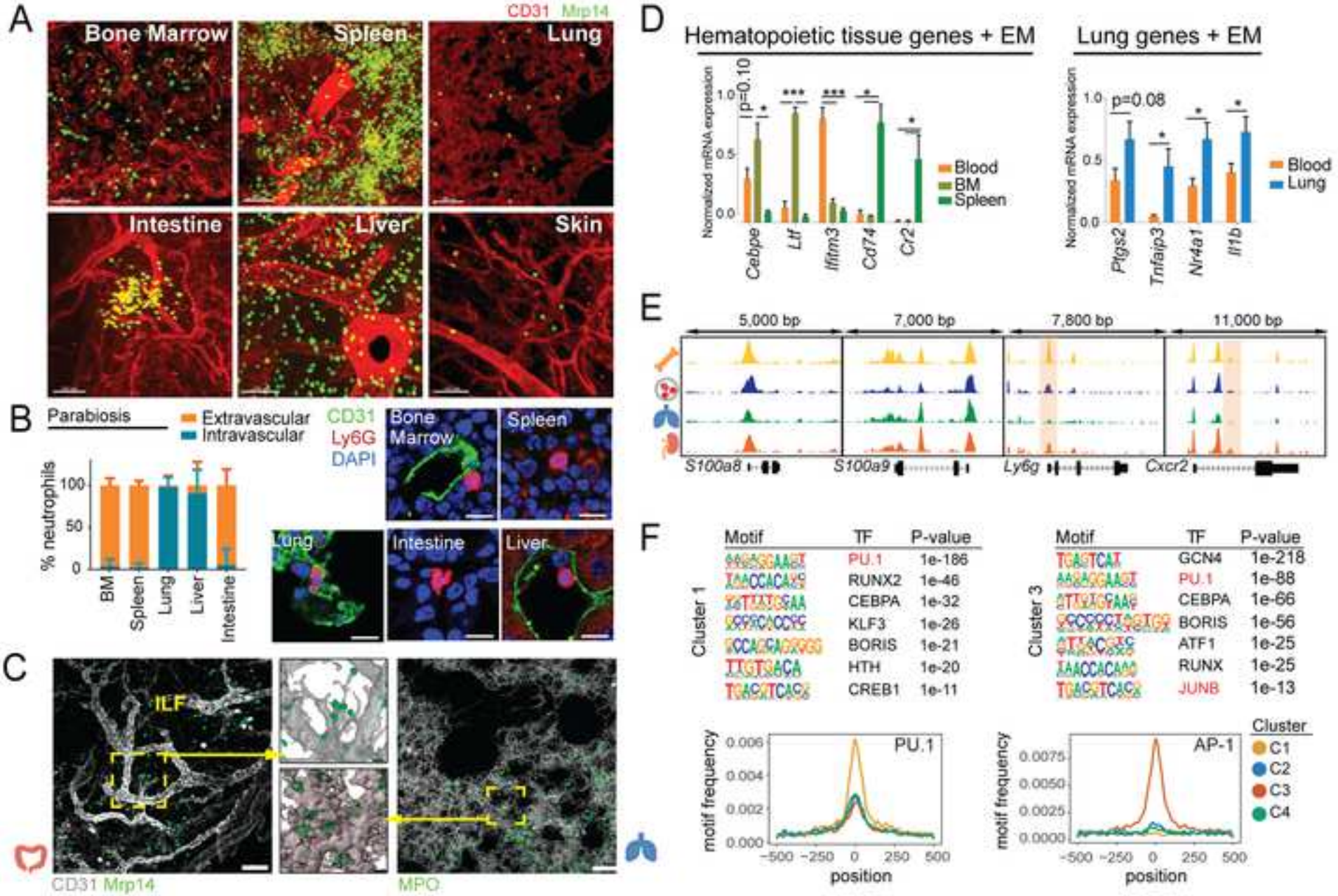

FigS4

Click here to access/download;Supplemental Figure;FigS4_imprinting_New-01.tif

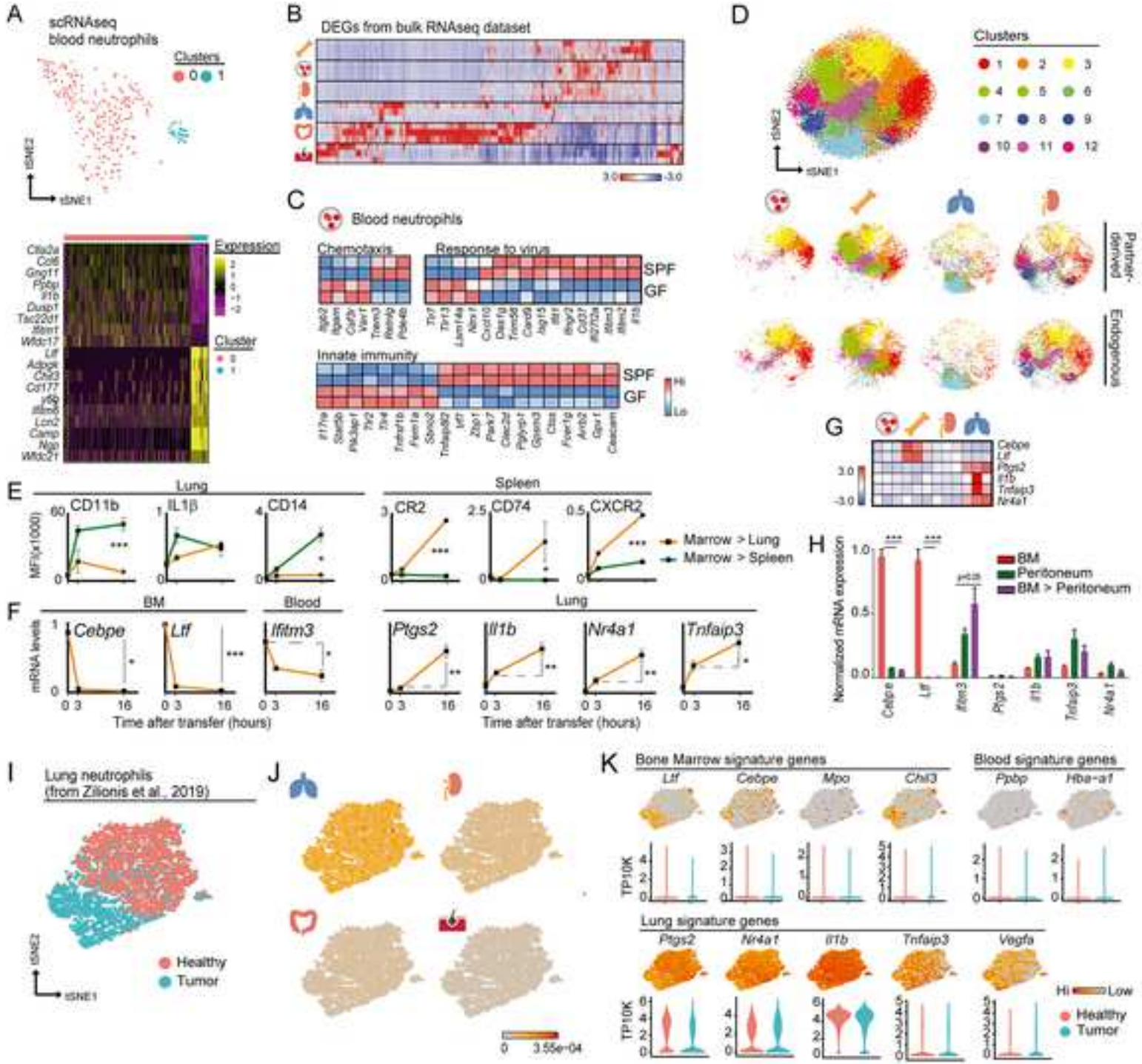

FigS5

Click here to access/download;Supplemental Figure;FigS5_leuko + angio-01.tif

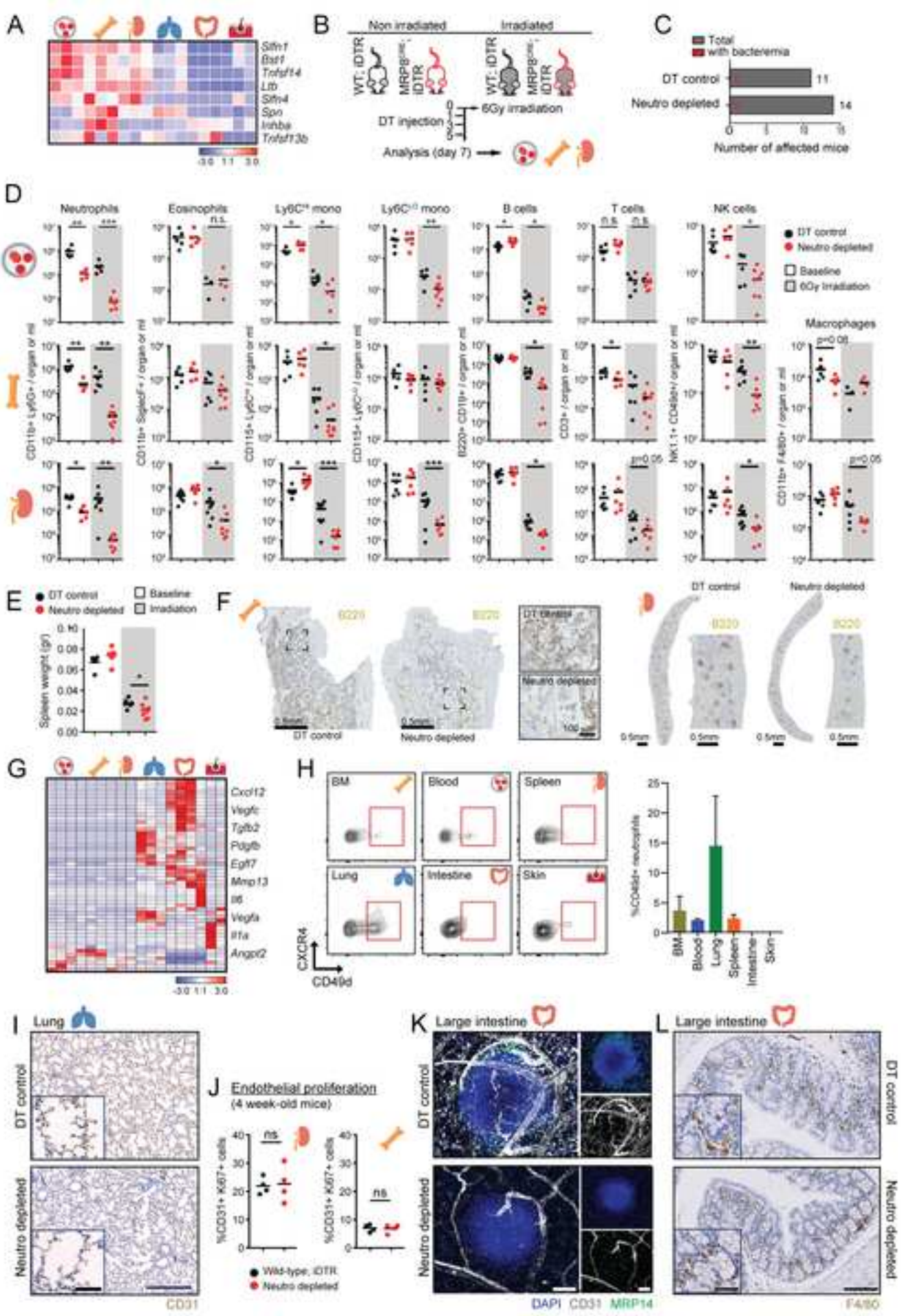

FigS6

Click here to access/download;Supplemental Figure;FigS6_CXCR4_New-01.tif

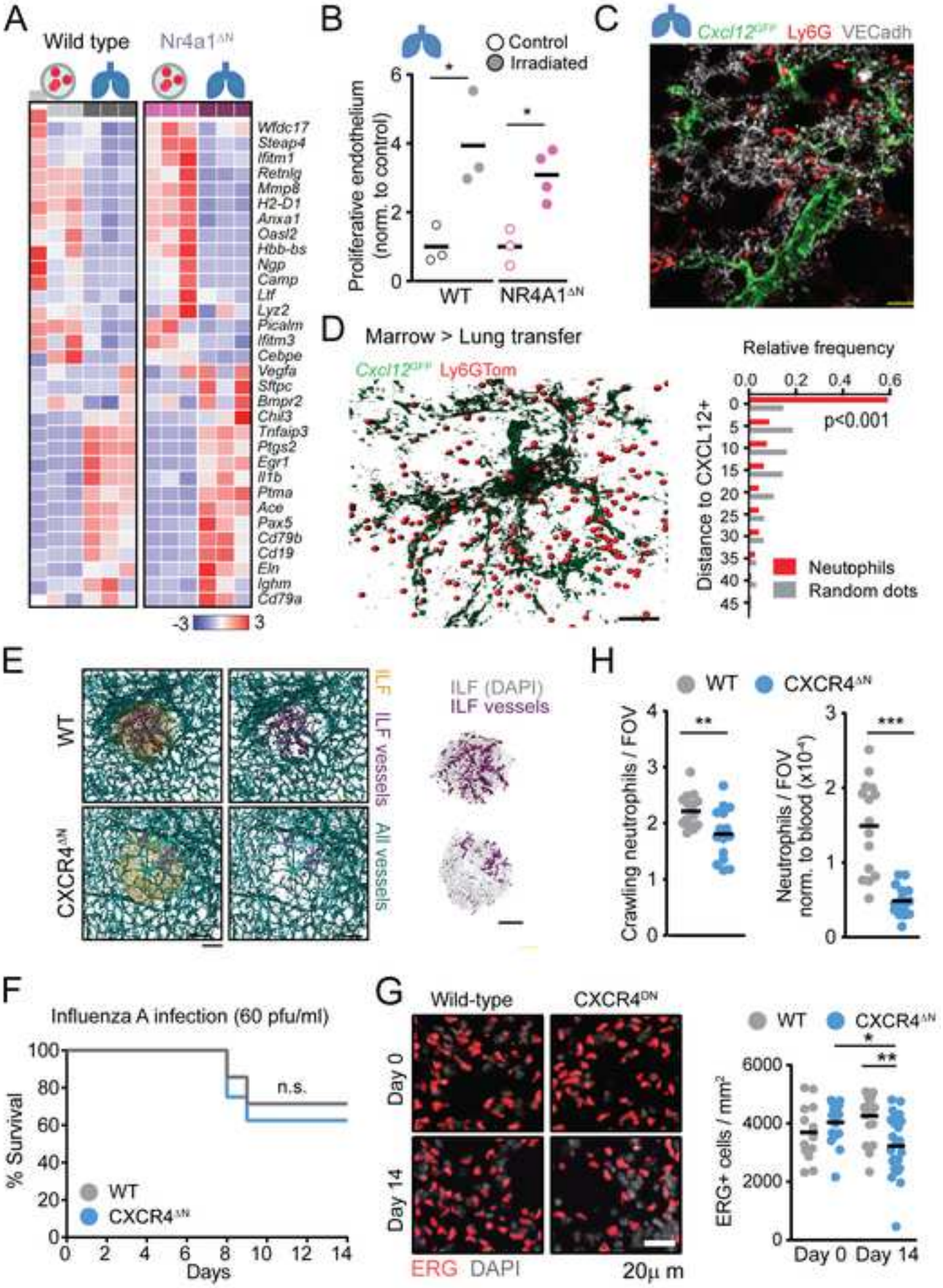

Video S1. Intravascular crawling of wild type and CXCR4N Ly6G+ neutrophils (grey) in the lung capillaries by intravital imaging

Table S1. DEG single cell RNAseq

Click here to access/download

Supplemental Videos and Spreadsheets

Supl Table 1.xlsx

Table S2. DEGs bulk RNA-sequencing and ATAC-sequencing analysis

Click here to access/download

Supplemental Videos and Spreadsheets

Supl Table 2.xlsx

Table S3. DEGs germ-free

Click here to access/download

Supplemental Videos and Spreadsheets

Supl Table 3.xlsx

Table S4. Pathway analysis

Click here to access/download

Supplemental Videos and Spreadsheets

Supl Table 4.xlsx

Table S5. Angiogenic gene list used for the angiogenic score and nanostring profiling

Click here to access/download

Supplemental Videos and Spreadsheets

Supl Table 5.xlsx